Nano Research

Open Access

Review Article

Carbon-supported single-atom materials for photovoltaic applications

Zhuo Dong[1,§], Yan Wu[1,§], Wajeeha Fatima[1], Wenqi Lyu[1], Chengrui Peng[1], Meng He[2,3], Xiong Yin[1]✉, and Leyu Wang[1]✉

[1] *State Key Laboratory of Chemical Resource Engineering, Innovation Centre for Soft Matter Science and Engineering, Beijing University of Chemical Technology, Beijing 100029, China*
[2] *National Center for Nanoscience and Technology, Beijing 100190, China*
[3] *University of Chinese Academy of Sciences, Beijing 100049, China*
[§] *Zhuo Dong and Yan Wu contributed equally to this work.*

Cite this article: *Nano Research*, **2026**, *19*, 94908473. https://doi.org/10.26599/NR.2026.94908473

ABSTRACT: Carbon-supported single-atom materials (CSAMs) have emerged as a revolutionary class of materials due to their exceptional atomic efficiency, high catalytic activity and tunable electronic properties. Although CSAMs have made significant contributions to catalysis and energy storage, their mechanistic roles in photovoltaic applications remain underexplored. This review systematically examines the device structures, working principles and current challenges of dye-sensitized solar cells, quantum dot solar cells and perovskite solar cells, alongside the pivotal functions of CSAMs in photovoltaics. Featuring atomically dispersed active sites, unique coordination environments, and modifiable electronic structures, CSAMs offer innovative solutions to inherent efficiency and stability limitations in photovoltaic devices. How the electronic structure of metal single-atoms, coordination environments and interactions between CSAMs and photovoltaic materials influence charge separation, transport, injection and catalytic processes in solar cells is elucidated in this review, which establishes a critical bridge between the rapidly evolving field of CSAMs and the development of high-performance, cost-effective solar cells.

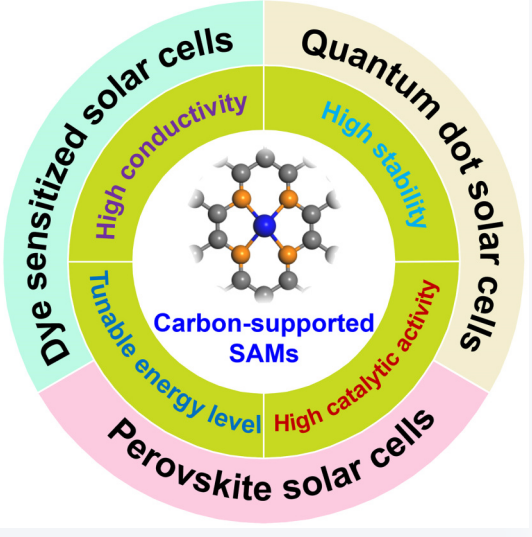

KEYWORDS: carbon-supported single-atom materials, energy storage, photovoltaics, dye-sensitized solar cells, quantum dot solar cells, perovskite solar cells

1 Introduction

Solar cells, as a critical component of clean energy technology, are undergoing a transition from traditional silicon-based cells toward novel, high-efficiency and low-cost alternatives. Representing the third generation of photovoltaic technologies, dye-sensitized solar cells (DSCs), quantum dot solar cells (QDSCs), and perovskite solar cells (PSCs) have garnered significant attention due to their advantages of simple fabrication processes, low raw material costs and tunable optoelectronic properties [1–6]. However, the large-scale commercialization of these technologies still faces substantial challenges, primarily including the high cost of precious metal electrodes, inadequate long-term device stability and limitations in charge transport efficiency [7–9].

In recent years, carbon-supported single-atom materials (CSAMs) have emerged as revolutionary materials. By anchoring individual metal atoms onto carbon supports, CSAMs achieve maximized atomic utilization efficiency and precise electronic structure modulation [10, 11]. Although CSAMs have become research hotspots in fields such as energy storage [12], catalysis [13], environmental protection [14], and biomedicine [15], their application in photovoltaic devices remains underexplored. CSAMs exhibit immense potential in addressing critical challenges in next-

Received: November 19, 2025; **Revised:** January 16, 2026
Accepted: January 21, 2026

✉Address correspondence to Xiong Yin, yinxiong@mail.buct.edu.cn; Leyu Wang, lywang@mail.buct.edu.cn

generation solar cells owing to their atomically dispersed active sites, tunable electronic structures, exceptional electrical conductivity and chemical stability and non-precious metal composition [16–19].

Specifically, the application of CSAMs in photovoltaics has evolved into an active research frontier. In DSCs and QDSCs, a prominent trend involves replacing the expensive and unstable Pt counter electrode (CE). Recent studies have shown that CSAMs based on non-precious metals (e.g., Fe, Co, Ni) can achieve superior catalytic activity for the I_3^-/I^- redox couple compared to Pt, with their 100% atomic utilization directly addressing resource scarcity concerns [20, 21]. Current research is advancing beyond simple substitution, delving into how precise modulation of the coordination environments of single metal atoms can optimize the adsorption energy of electrolyte species, thereby fundamentally enhancing the redox couple reaction kinetics in the electrolyte [22–27]. Similarly, in PSCs, CSAMs are employed as multifunctional interfacial layers. The atomically dispersed active sites have been demonstrated to effectively passivate interfacial defects between the perovskite layer and charge transport layers, significantly reducing non-radiative recombination losses of charge carriers [28–31]. Furthermore, the interactions between single metal atoms and the carbon support are being actively exploited to tailor the electronic properties of CSAMs, optimizing energy level alignment and charge extraction between the perovskite layer and charge transport layers [32–34]. This inherent designability, coupled with the stabilizing effect of carbon supports in suppressing metal atom aggregation, enables CSAMs to serve as a class of multifunctional materials capable of not only enhancing the power conversion efficiency (PCE) but also addressing long-standing stability challenges of photovoltaic devices [35].

This review systematically examines the structures, operating principles, and major challenges of three emerging photovoltaic devices (DSCs, QDSCs, and PSCs). It also provides the first comprehensive and systematic exploration of the pivotal roles played by CSAMs in addressing the key challenges faced by DSCs, QDSCs and PSCs. The inherent atomically dispersed active sites, unique coordination structures, and tunable electronic properties of CSAMs offer innovative approaches to overcoming the intrinsic efficiency and stability limitations of photovoltaic devices. This review aims to elucidate how the electronic structure and coordination environment of single metal atoms in CSAMs, along with their interactions with the support, influence carrier separation and transport, catalytic processes and material stability in solar cells.

2 Advantages and synthesis of CSAMs

In the field of photovoltaics, the emergence of CSAMs has provided new possibilities for addressing key issues such as interfacial charge transport and catalytic reaction kinetics. The sophisticated synthesis methods of these materials are inseparable from their unique properties, and together they determine the final performance of photovoltaic devices.

2.1 Advantages of CSAMs

Carbon materials have long held a significant position in the field of energy conversion and storage due to their unique physical and chemical properties [16]. Their basic structural unit consists of sp^2-hybridized carbon atoms, which can form multidimensional structures such as graphite, graphene, and carbon nanotubes through different arrangements, exhibiting excellent electrical conductivity, abundant specific surface area, and tunable surface chemical properties [36]. These characteristics make carbon materials ideal electrode and support materials. However, traditional carbon materials have limitations in the design of atomic-level active sites and the regulation of interfacial interactions, often making their intrinsic catalytic activity and selectivity insufficient to meet the stringent requirements of high-performance optoelectronic devices. The development of CSAMs aims to overcome these limitations. By anchoring metal centers onto carbon substrates at the atomic scale, CSAMs not only fully inherit the excellent conductivity and stability of carbon materials but also generate a series of unique enhancement characteristics inherent to single-atom sites [37–39].

The core properties of CSAMs originate from their unique atomic-level structural characteristics. Maximum atomic utilization efficiency and tunable electronic structure are their most fundamental advantages [40]. Since metals exist as isolated single atoms, each metal atom becomes a fully exposed active site, achieving a theoretical 100% atomic utilization efficiency [41]. More importantly, the electronic structure of individual metal atoms is closely related to their local coordination environment [42]. By adjusting the types of coordinating atoms or introducing defects, their energy level structure and surface adsorption properties can be precisely regulated, thereby optimizing their functionality in specific application scenarios [43, 44]. This tunability provides broad space for the precise design of material properties. Well-defined active sites and strong metal–support interactions ensure the reliability of the materials in practical applications. Uniform M-N-C active centers eliminate the intrinsic activity differences caused by size disparities in traditional nanocatalysts, providing an ideal platform for in-depth studies of catalytic mechanisms [45]. At the same time, the strong chemical bonding formed between metal atoms and the carbon support effectively prevents the migration and agglomeration of single atoms during service, ensuring the long-term stable operation of devices [46]. These structural features collectively contribute to the excellent mass transfer efficiency and interfacial compatibility of the materials, enabling them to maintain stable performance output even under complex working conditions [47]. Excellent charge transport capability and energy level compatibility give them unique advantages in photovoltaic devices [48]. The carbon substrate itself has good conductivity, providing an ideal channel for charge transport [49]. The single-atom sites, through their tunable work function, can optimize energy level matching with adjacent functional layers [50]. This energy level adaptability can significantly reduce interfacial barriers, promote the efficient extraction and transport of photogenerated carriers, and effectively reduce energy loss, offering new solutions for improving device performance [51].

2.2 Synthesis of CSAMs

The synthesis strategies for CSAMs show a trend of diversified development. Atomic layer deposition (ALD), with its vapor-phase deposition characteristics, enables precise anchoring of single atoms through self-limiting reactions of precursor gases on the support surface [52, 53]. Although this method offers extremely high precision control and enables the construction of well-defined active sites, its high equipment costs and complex process requirements limit its application in large-scale production [54]. In contrast, wet chemistry methods achieve single-atom dispersion

by interacting metal precursors with functionalized carbon supports in the solution phase, followed by post-treatment thermal processes [55]. The advantages of this method lie in its relatively simple process flow, lower cost, and potential for scale-up production, making it one of the most commonly used synthesis strategies today [56, 57]. Pyrolysis, as the mainstream method for preparing carbon-supported single-atom catalysts, typically uses precursors such as metal-organic frameworks (MOFs) for high-temperature thermal treatment in an inert atmosphere [58]. This method cleverly utilizes bimetallic strategies or spatial confinement effects to effectively prevent the agglomeration of metal atoms during high-temperature processes, demonstrating good cost-effectiveness and industrial prospects [59, 60]. Meanwhile, ball milling, as a mechanochemical method, directly disrupts chemical bonds through the mechanical forces generated by high-energy ball milling, embedding metal atoms into the carbon matrix [61, 62]. This green and efficient synthesis pathway opens new possibilities for the scalable preparation of single-atom catalysts [63].

In summary, the development of CSAMs is transitioning from the exploration of synthesis methods to the precise regulation of performance. Through the realization of diversified synthesis strategies and an in-depth understanding of unique characteristics, the application prospects of these materials in photovoltaic devices will become even broader.

3 Structure of photovoltaic devices

3.1 Dye-sensitized solar cells

In 1991, Michael Grätzel's team utilized nanoporous TiO_2 electrodes and ruthenium-based dyes to achieve 7% of PCE, establishing the foundation for DSCs [64]. Subsequent optimization of electrolytes and dyes enabled DSCs to reach 32% efficiency under low-light conditions (theoretical efficiency limit: 35%), however, their performance under strong light remains inferior to that of silicon cells with a current maximum efficiency of ~ 14% [65]. The light-harvesting materials primarily comprise organic dyes, metal complexes (e.g., ruthenium-based or natural dyes) [66]. The semiconductor electrode typically consists of mesoporous TiO_2 due to its excellent conductivity, chemical stability and high dye adsorption capacity [67]. The electrolyte is usually a polyiodide solution (I^-/I_3^-) that supplies electrons to the dye [68]. The CE, often made of noble metals like Pt, collects electrons and facilitates electrolyte reactions [69]. The structure of DSC is shown in Fig. 1(a) [70]. In operation, dyes absorb photons to generate excited electrons, which are injected into the TiO_2 conduction band and then travel via an external circuit to the CE. The electrolyte then accepts these electrons to reduce and regenerate the oxidized dye, completing the solar energy conversion cycle [71], as shown in Fig. 1(b). Compared to silicon cells, DSCs offer lower costs and simpler fabrication. A key limitation is the inadequate stability of Pt-based CEs in catalyzing polyiodide redox reactions, alongside the high-cost hindering commercialization [72].

3.2 Quantum dot solar cells

QDSCs emerged in the early 2000s as an evolution of DSC structures, integrating quantum dots (QDs) unique properties with sensitized solar cell design principles. Researchers replaced dyes with inorganic QDs like PbS, CdSe, CdS and InP, enabling absorption spectrum tuning via size control [73–76]. Exceptional light absorption, multiple exciton generation, and adjustable bandgaps endow QDSCs with a theoretical efficiency limit of 44%,

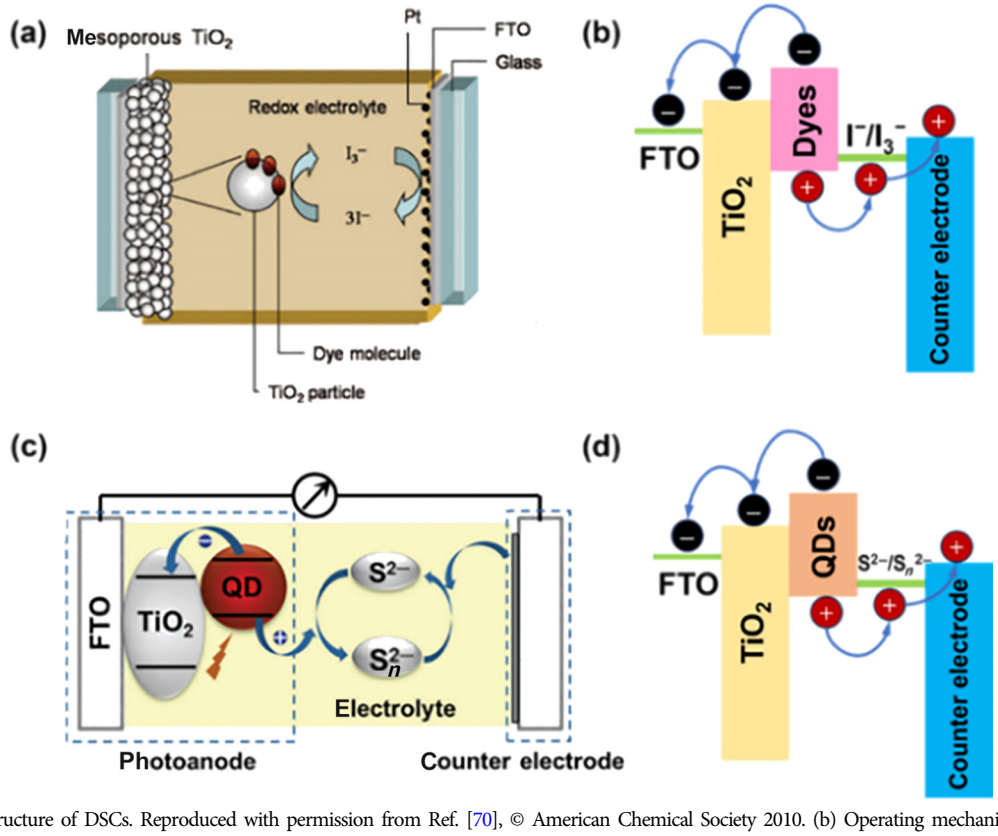

Figure 1 (a) The structure of DSCs. Reproduced with permission from Ref. [70], © American Chemical Society 2010. (b) Operating mechanism of DSCs. (c) The structure of QDSCs. (d) Operating mechanism of QDSCs. Reproduced with permission from Ref. [78], © Royal Society of Chemistry 2018.

surpassing that of all other single-junction photovoltaic technologies [77]. A typical QDSC comprises a QD-sensitized photoanode, a polysulfide electrolyte (S^{2-}/S_n^{2-}) and a catalytic cathode (Fig. 1(c)) [78]. Its working mechanism parallels that of DSCs: QDs absorb photons to excite electrons into their conduction band; these electrons are injected into the TiO_2/FTO conduction bands and then collected externally. Simultaneously, the holes in the valence band of QDs are regenerated by the reduced substances in the electrolyte, and the electrons in the CE reduce the oxidized electrolyte in the electrolyte to complete a photoelectrochemical cycle, as shown in Fig. 1(d). Studies have confirmed that the catalytic cathode significantly impacts the PCE of QDSCs [79]. Common CE materials include noble metals (Pt, Au), metal sulfides (CoS_2, Cu_2S, CuS), carbon materials (graphene, carbon nanotubes, carbon black) and conductive polymers (PANI, PPy, PEDOT) [80–83]. Advancing the commercialization of QDSCs requires balancing environmental friendliness, cost, performance and stability. Thus, developing simple, low-cost, non-toxic CEs with high catalytic activity and conductivity for polysulfide reduction reactions (SRR) is critical for improving efficiency [84].

3.3 Perovskite solar cells

In 2009, Japanese scientist Miyasaka first utilized $CH_3NH_3PbI_3$ as a photosensitizer to replace dye, depositing it onto TiO_2 mesoporous films and achieving a PCE of 3.8% [85]. However, liquid electrolytes severely constrained the stability and PCE of PSCs. Consequently, in 2012, Park's team developed a solid-state hole transport layer, enabling the PCE of PSCs to surpass 9% [86]. Over the subsequent decade, PSCs experienced rapid efficiency advancements, with the PCE of single-junction devices approaching 27%—exceeding silicon solar cells—establishing PSCs as the most promising candidate in third-generation photovoltaics [87]. The ABX_3-structured perovskite materials (A: FA^+, MA^+, Cs^+; B: Pb^{2+}, Sn^{2+}; X: Cl^-, Br^-, I^-) exhibit exceptional light absorption, long carrier lifetimes and low material costs, positioning PSCs as strong competitors to silicon-based solar cells for large-scale commercialization [88, 89]. PSCs are primarily categorized into two device architectures: mesoscopic and planar. Mesoporous structure refers to the perovskite layer filled in mesoporous materials (such as mesoporous TiO_2, Al_2O_3, ZrO_2), as shown in Fig. 2(a) [90]. The preparation process of mesoporous layers requires high-temperature sintering, limiting their large-scale production [91]. The planar heterojunction structure directly sandwiches the perovskite layer between the electron and hole transport layers without mesoporous scaffolds, offering simplicity suitable for large-scale applications [92]. Planar PSCs are further categorized based on the carrier transport direction: at the bottom and top of the perovskite layer, the conventional (n–i–p) PSCs (Fig. 2(b)) employ electron transport layer (ETL) materials (e.g., SnO_2, TiO_2 and ZnO) and hole transport layer (HTL) materials (e.g., Spiro-OMeTAD and PTAA), respectively, while the inverted (p–i–n) ones (Fig. 2(c)) utilize HTL materials (e.g., self-assembled monolayer (SAM) and PEDOT:PSS) and ETLs based on fullerenes and their derivatives (e.g., C_{60} and PCBM) [93–97]. Despite the differences in charge transport layers, the fundamental working principles remain identical for both the conventional and inverted PSCs. This has further led to the development of PSCs with novel structures such as carbon-electrode perovskite solar cells (C-PSCs) and HTL-free C-PSCs (Fig. 2(d)) [32, 98]. The operational process comprises: (1)

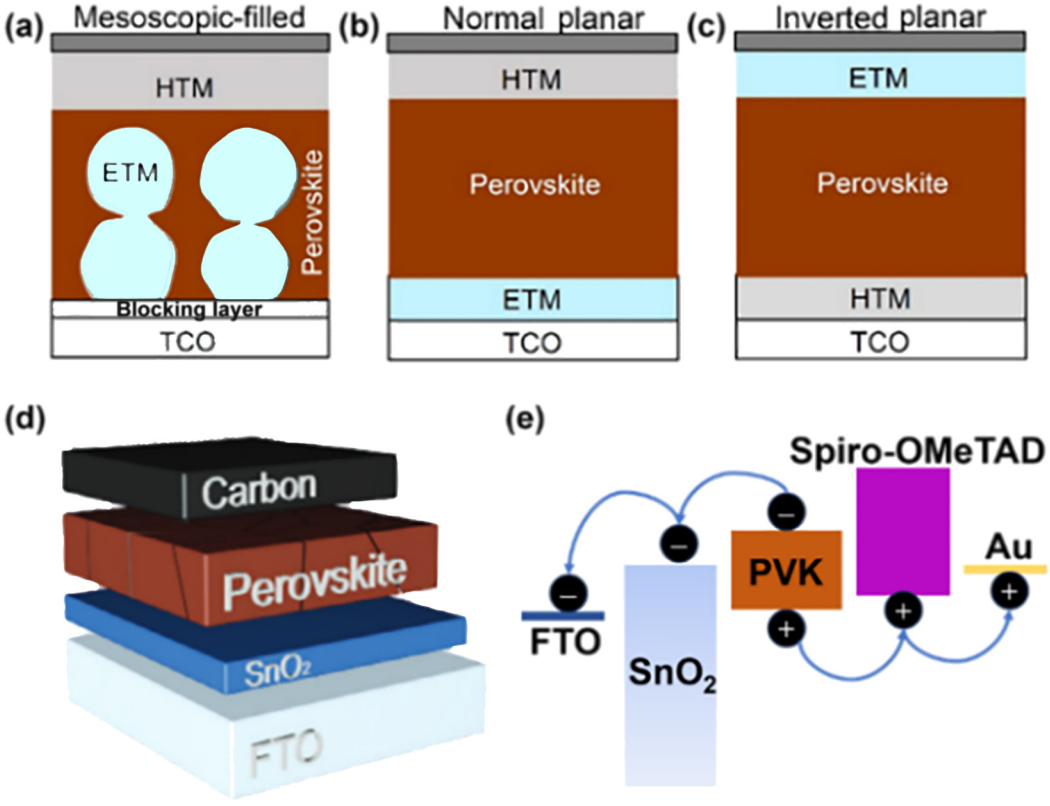

Figure 2 PSCs with (a) mesoscopic, (b) normal-planar, and (c) inverted-planar device structures. Reproduced with permission from Ref. [90], © American Chemical Society 2020. (d) Schematic diagram of planar HTL-free C-PSCs. Reproduced with permission from Ref. [99], © Wiley-VCH GmbH 2024. (e) Working principle of PSCs.

photon absorption by the perovskite active layer generating electron–hole pairs; (2) exciton separation under built-in electric fields; (3) carrier diffusion to ETL/HTL interfaces; (4) charge transport through respective layers; and (5) electrode collection (Fig. 2(d)) [99].

At present, there are two crucial issues restricting the performance and stability of PSCs. Firstly, during the crystallization process of perovskite thin films, high-density defects are inevitably generated [100]. The presence of bulk defects can alter the p-type or n-type characteristics of the perovskite thin films. Moreover, the defect density at the interface of perovskite thin films is two orders of magnitude higher than that in the bulk phase. These high-density interface defects act as non-radiative recombination centers during the carrier transfer process, significantly reducing the open-circuit voltage (V_{oc}) and fill factor (FF) of PSCs [101]. Consequently, passivating the interface defects has become a key factor in enhancing the performance of PSCs. In addition, halide ions in the perovskite layer are highly susceptible to lattice detachment under the influence of light, heat and electrical stimuli [102, 103]. As a result, defect sites become migration channels for halide ions, accelerating the degradation rate of perovskite thin films and severely limiting the stability of PSCs [104]. Secondly, the commonly employed metal electrodes (such as Au, Ag and Cu) in traditional PSCs are the primary causes of device degradation. The migration of halide ions in the perovskite layer can penetrate the charge transport layer and damage the metal electrodes [105, 106]. Therefore, replacing traditional metal electrodes with carbon-based electrodes is regarded as an effective strategy to enhance the stability of PSCs. However, compared to traditional PSCs, the photovoltaic performance of carbon-based perovskite solar cells remains relatively low [107]. This is mainly attributed to the poor electrical conductivity and electron mobility of the carbon electrode layer [108], as well as the poor contact at the perovskite/carbon interface and the energy level mismatch between the carbon electrode and adjacent layers [109]. Therefore, regulating the carrier transport process of carbon electrode materials and minimizing energy losses are of utmost importance.

4 CSAMs in dye-sensitized solar cells

In DSCs, the CE material plays a critical role in catalyzing the iodide redox reaction (IRR). Although traditional noble metal catalysts like Pt exhibit good activity, their high cost and inherent stability issues significantly hinder large-scale commercial application. This practical challenge has driven researchers to explore next-generation catalytic materials, among which CSAMs have emerged as highly promising alternatives due to their unique atomically dispersed nature, tunable electronic structure, and excellent electrical conductivity.

Maximizing the atomic utilization efficiency of noble metals represents a critical strategy to balance high performance and low cost. Li's team successfully combined Pt single atoms with phase-pure molybdenum carbide (α-MoC) anchored carbon sphere flowers (Pt/α-MoC@CS) [23]. The SEM and Transmission Electron Microscope (TEM) images in Figs. 3(a) and 3(b) show the spherical flower-like hollow structure of α-MoC@CS. High-resolution transmission electron microscope (HRTEM) images and the corresponding selected area electron diffraction (SAED) pattern in Figs. 3(c) and 3(d) further confirm the crystalline characteristics of this material. The element mapping in Fig. 3(e) clearly shows the uniform distribution of Pt atoms. This meticulous structural design resulted in excellent photovoltaic performance; *J*–*V* curves in Fig. 3(f) show that the device based on Pt/α-MoC@CS achieved a PCE of 9.67%. In-depth theoretical analysis indicated that electrons transfer from the α-MoC support to the Pt atoms, as evidenced by the differential charge density plot shown in Fig. 3(g). The adsorption free energy calculations in Fig. 3(h) and the crystal orbital Hamilton population (COHP) analysis in Fig. 3(i) jointly reveal the intrinsic mechanism for the performance enhancement: the optimized electronic structure brings the adsorption free energy of I^- closest to the ideal value while reducing the binding strength with reaction intermediates.

Among the various single-atom materials, cobalt-based catalysts have been the most systematically studied. Zhou et al. developed N-doped carbon-supported cobalt single-atom catalysts (Co-NC SACs) derived from a MOF compound and applied them in DSSCs as CEs, achieving a PCE of 9.25%, which significantly outperform traditional Pt electrodes [110]. The performance enhancement was attributed to the strong adsorption capability of Co-N_x sites for I-3 and low desorption energy barrier for I^-, which synergistically optimize the reaction kinetics. Bao's team further confirmed that among a series of 3d transition metal (Mn, Fe, Co, Ni, Cu) SACs embedded into graphene nanosheets (GN), the CoN_4/GN structure exhibited the highest catalytic activity toward IRR, primarily due to its optimal adsorption-desorption balance [111]. As shown in Fig. 4(a), the device based on CoN_4/GN demonstrated significantly superior performance compared with other reference samples.

Notably, the precise modulation of the local coordination environment of cobalt atoms can lead to substantial improvements in catalytic performance. Shi's group constructed Co–S bonding configuration on sulfur-doped carbon supports [112]. As clearly shown in Figs. 4(b) and 4(e) the Co-S/C-SAC sample exhibited an irregular porous structure composed of thin carbon sheets, and high-angle annular dark field scanning transmission electron microscopy (HAADF-STEM) images confirmed the uniform distribution of high-density Co single atoms within the porous carbon framework. This unique structural characteristic is closely linked to its excellent electrochemical performance. The cyclic voltammetry (CV) results in Fig. 4(f) show that Co-S/C-SAC possessed the smallest peak-to-peak separation (E_{pp}) and the largest peak current density (J_{cp}), demonstrating optimal IRR catalytic activity. Photovoltaic performance tests in Fig. 4(g) revealed that devices using Co-S/C-SAC as CEs achieved an efficiency of 8.18%, superior to that of the cell with a Pt-based CE. Stability tests in Figs. 4(h) and 4(i) further confirmed the outstanding electrochemical durability of this material.

Furthermore, the same group constructed a Co-N_3-V structure with vacancies. Density functional theory (DFT) calculations revealed enhanced I_2 adsorption capability and accelerated electron transfer processes [113]. Chen's group innovatively introduced phosphorus atoms to create P, N co-coordinated cobalt sites ($Co/Co_1P_1N_3$) [114]. They found that P-coordination significantly weakened the interaction between cobalt and iodide ions, effectively promoting the desorption of reaction products. This discovery provides crucial insights for the rational design of single-atom catalysts.

The universality of the CSAM strategy has been validated in various metal systems, including Ti, Fe, Ni and Mo. Shi's group introduced a single-atom Ti catalyst into reduced graphene oxide (rGO) by chemically adsorbing Ti atoms on oxygenated sites of rGO, referred to as Ti_1/rGO (Fig. 5(a)) [26]. The structural

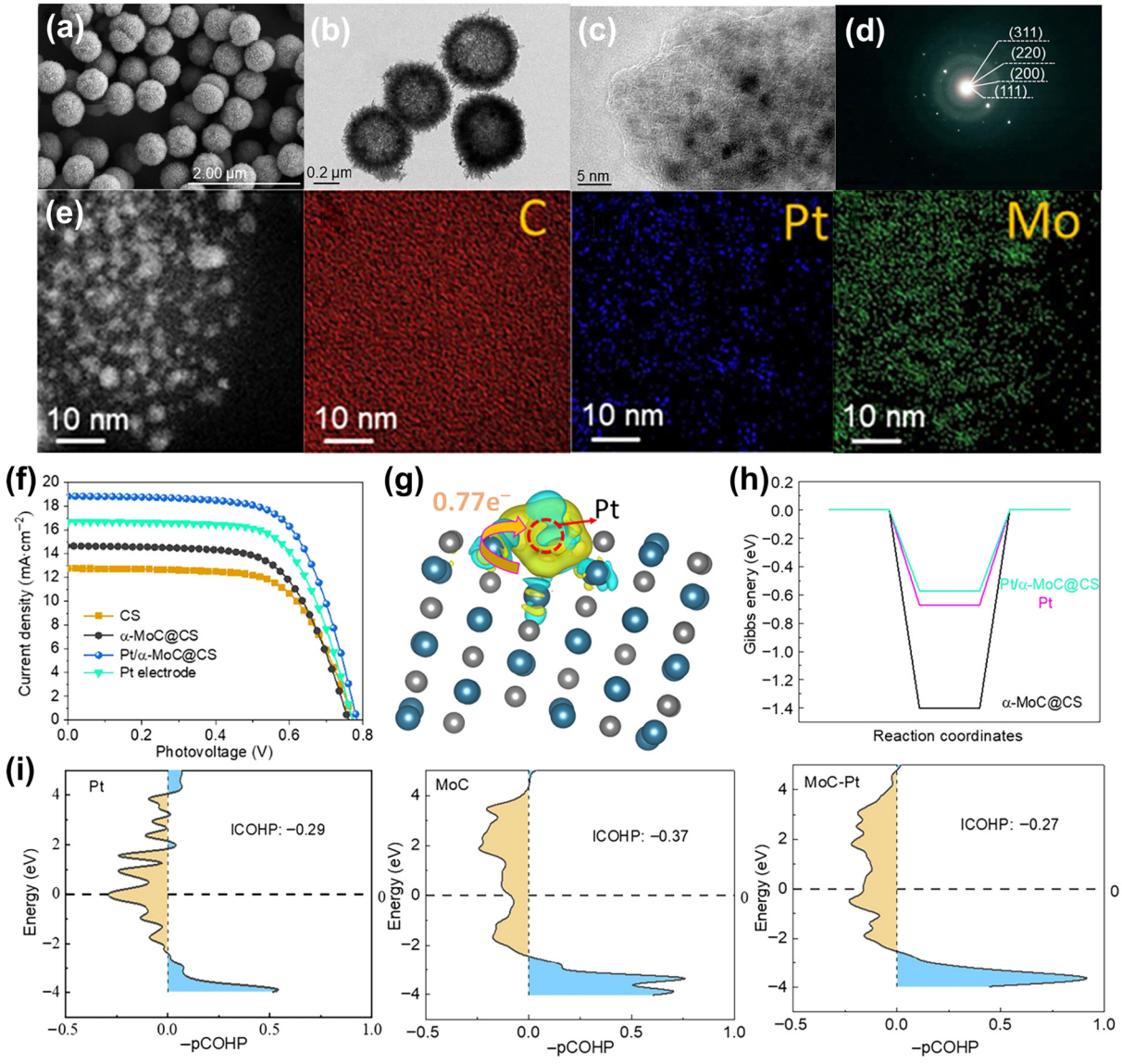

Figure 3 (a) SEM image of α-MoC@CS. (b) TEM image of α-MoC@CS. (c) HRTEM image of Pt/α-MoC@CS. (d) The SEAD pattern of α-MoC@CS. (e) HAADF-STEM image and corresponding element mapping images of Pt/α-MoC@CS. (f) *J*–*V* curves of DSCs with different CEs. (g) Differential charge density for Pt/α-MoC@CS. (h) Gibbs free energy diagram for I^- adsorption on α-MoC and α-MoC-Pt and Pt (111) surfaces. (i) COHP of Pt, α-MoC and α-MoC-Pt. Reproduced with permission from Ref. [23], © Elsevier Ltd. 2023.

characterization in Figs. 5(b)–5(g) confirms the uniform distribution of Ti atoms on the rGO. The IRR catalytic activity of Ti_1/rGO e was further assessed. As shown in Fig. 5(h), Ti_1/rGO exhibits the smallest E_{pp} and the highest J_{cp}, indicating outstanding catalytic performance for the IRR. Electrochemical impedance spectroscopy (EIS) was further employed to elucidate the electrochemical kinetics of Ti_1/rGO (Fig. 5(i)). The charge transfer from the cathode interface to the electrolyte during the IRR process corresponds to the first semicircle in the Nyquist plot. Notably, Ti_1/rGO exhibits the smallest first semicircle, indicating the minimal charge transfer resistance (R_{ct}). Ultimately, Ti_1/rGO was tested as a photoelectrode in DSCs. As shown in Fig. 5(j), the Ti_1/rGO-based DSC delivers the best PCE, significantly higher than those of devices based on both Pt-CE and rGO-CE.

This group also employed an *in situ* grafting strategy to partially stabilize atomic titanium nitride (Ti_1N_2OH) onto a layered, mesoporous carbon support, forming Ti_1/NC-SAC [115]. The DSC based on Ti_1/NC-SAC demonstrated an excellent PCE of 8.2%, comparable with that of the Pt-based DSC (8.3%). Additionally, steady-state output tests performed for Ti_1/NC-SAC and NC-based DSCs showed PCEs stable at 7.92% and 5.90%, respectively, closely matching the *J*–*V* measurement results. These findings suggest that introducing Ti single atoms effectively enhances the IRR catalytic activity, improving the photovoltaic performance and stability of DSCs.

The iron-based single-atom catalyst reported by Yun's team and the nickel-based single-atom catalyst (Ni-SAC) developed by our research group both demonstrated comparable performance to Pt CE [22, 27]. The synthetic schematics in Figs. 6(a) and 6(b) illustrate the preparation processes and structural features of N-doped porous carbon loaded with Fe single atoms (Fe-ISAs/NPC) and Ni-SAC, respectively. The free energy diagram in Fig. 6(c) and the Kelvin probe force microscopy (KPFM) results in Fig. 6(d) together indicate that their superior performance stems from the

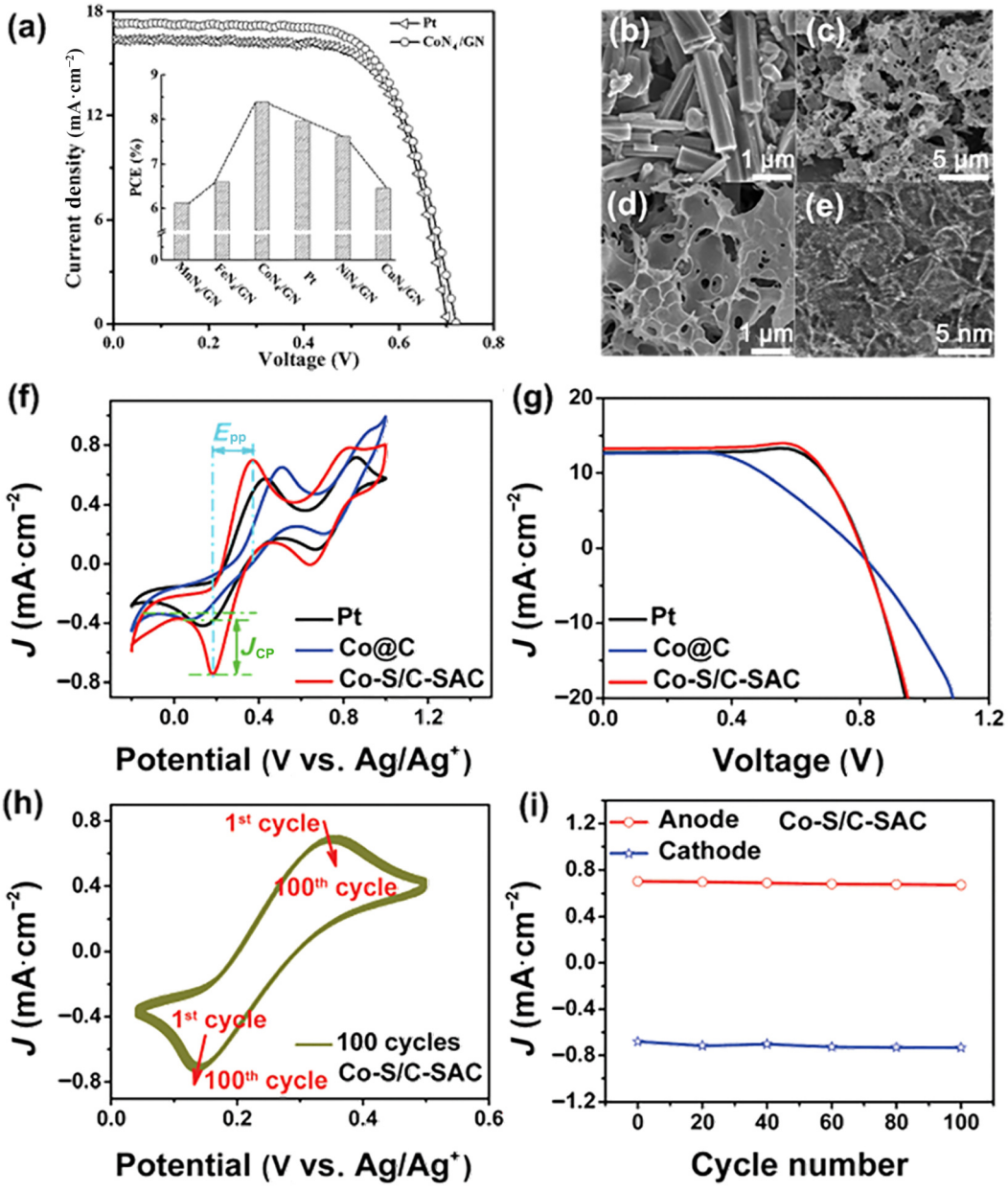

Figure 4 (a) Current density–voltage (J–V) curves of DSCs based on CoN_4/GN and Pt CEs. Inset: the measured PCEs of the DSCs fabricated with CEs from different MN_4/GN and Pt. Reproduced with permission from Ref. [111], © Wiley-VCH GmbH 2016. (b) SEM image of Co@C. (c) and (d) SEM of Co-S/C-SAC. (e) HAADF-STEM image of Co-S/C-SAC. (f) CV curves of Co-S/C-SAC, Co@C, and Pt in a liquid electrolyte system for DSCs. (g) J–V curves of DSCs using Pt, Co@C, and Co-S/C-SAC CEs. (h) 100 consecutive CV cycles of the Co-S/C-SAC-based CE in an electrolyte solution containing I_3^-/I^-. (i) Anodic and cathodic peak current density versus cycle number. Reproduced with permission from Ref. [112], © Royal Society of Chemistry 2021.

efficient adsorption at the single-atom sites and favorable energy level alignment with the redox couples. Particularly noteworthy is the molybdenum-based single-atom catalyst embedded within N-doped carbon support (Mo-N-C SAC) developed by our research group, which also exhibited excellent catalytic activity in a novel redox couple system [24]. The CV tests in Fig. 6(e) show the superior catalytic activity of Mo-N-C SAC toward the $Co^{2+/3+}(bpy)_3$ redox reaction. The photovoltaic performance in Fig. 6(f) and the energy level alignment analysis in Fig. 6(g) fully demonstrate the broad applicability of the design concept of single-atom catalysts in different systems.

To compare the performance enhancement of DSCs enabled by different CSAMs, we have systematically summarized the photovoltaic parameters of DSCs employing CSAM-based CEs with various metal centers in Table 1. A systematic analysis of the existing research reveals that the application of CSAMs as CEs for DSCs has transcended simple material replacement. The core value lies in enabling precise control over the catalytic process through atomic-level design. Maximized atom utilization efficiency and a tunable local coordination environment significantly enhance the intrinsic activity of the catalysts, while the strong chemical bonding between metal atoms and the carbon support ensures long-term material stability. These characteristics collectively establish the foundation for the large-scale application of CSAMs in DSCs, providing a clear technological pathway to overcome the limitations of traditional noble metal catalysts.

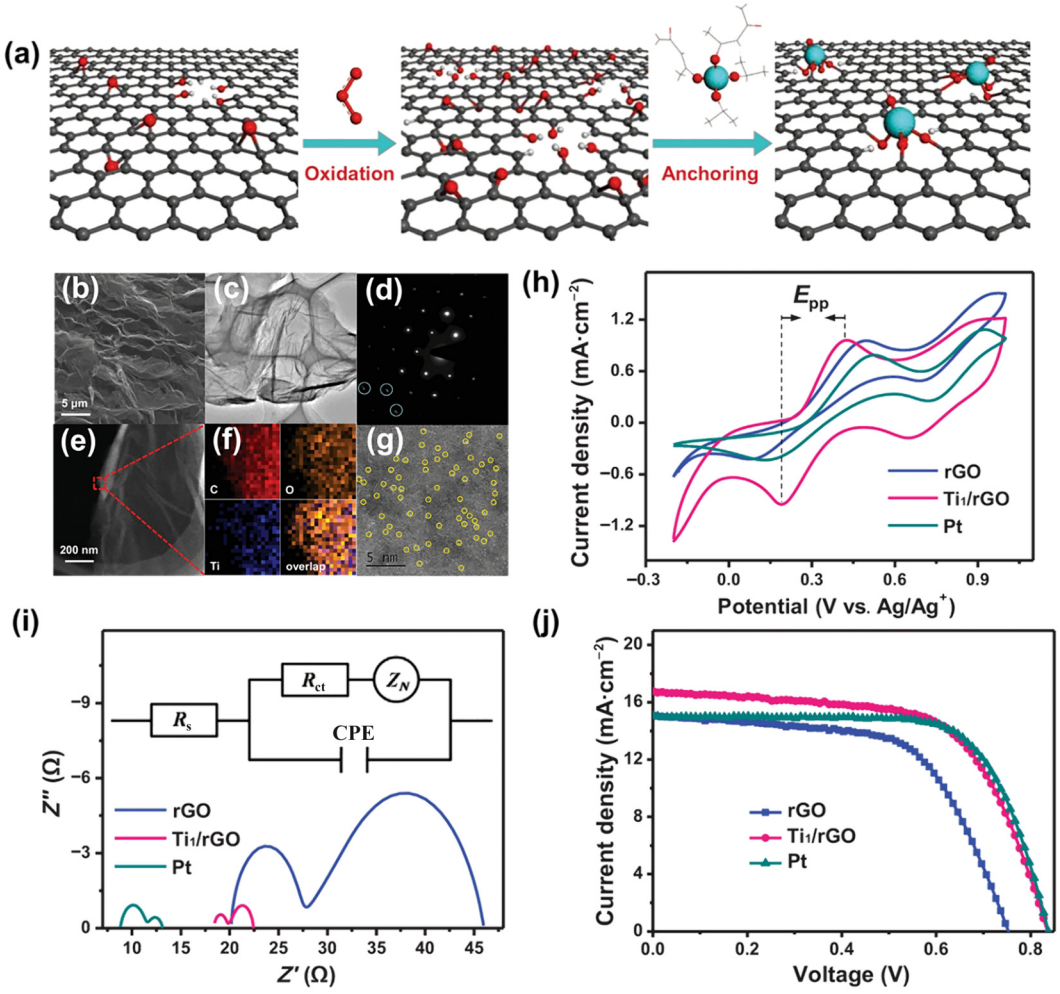

Figure 5 (a) Schematic illustration of the synthesis of Ti_1/rGO. (b) and (c) SEM images of Ti_1/rGO. (d) SAED pattern of Ti_1/rGO. (e) TEM image of Ti_1/rGO. (f) Element maps of Ti_1/rGO. (g) HAADF-STEM image of Ti_1/rGO. (h) CV curves of rGO, Ti_1/rGO, and Pt. (i) Nyquist plots of DSCs using various CEs. (j) *J*–*V* curves of DSCs using different CEs. Reproduced with permission from Ref. [26], © Wiley-VCH GmbH 2020.

5 CSAMs in quantum dot solar cells

Carbon materials are considered a highly promising class of CE materials for QDSCs [116]. Systematic studies have shown that materials such as mesoporous carbon, nitrogen-doped carbon and cobalt-nitrogen co-doped carbon can provide abundant catalytic sites for the polysulfide redox reaction and facilitate electron transport [117, 118]. Particularly when these carbon materials are combined with a highly conductive titanium mesh substrate featuring a three-dimensional grid structure, a robust catalytic layer up to sub-millimeter thickness can be constructed, significantly increasing the number of active sites and ultimately pushing the PCE of QDSCs beyond 13% [119].

Although heteroatom-doped carbon materials have achieved remarkable success, their catalytic active sites typically consist of randomly distributed dopant heteroatoms or the nanoclusters formed therefrom [120]. This limits the precise regulation of the electronic structure of the active sites and there is still a bottleneck in improving their intrinsic catalytic activity and atom utilization. To fundamentally break through this limitation, the research focus is gradually shifting towards designing the next generation of catalytic materials with well-defined and uniform active sites.

Consequently, CSAMs provide an unprecedented platform for precise regulation in optimizing the performance of CE in QDSCs. By precisely designing the type of metal center and its surrounding coordination environment, the adsorption/desorption behavior with polysulfide intermediates can be systematically modulated, thereby optimizing the reaction pathway and kinetics. This strategy opens up a promising avenue for addressing the slow kinetics of the SRR and improving the long-term stability of CEs, thereby potentially enhancing the performance of QDSCs.

Our research group employed a "coating-carbonization-etching" strategy to synthesize N-C shell-supported Fe- and Cu-based SACs, as well as N-C catalysts [25], as shown in Fig. 7(a). The HAADF-STEM images of the Fe-N-C sample revealed atomically dispersed Fe atoms within the carbon shell and element mapping confirmed the uniform distribution of all elements, as depicted in Figs. 7(b)–7(g). Additionally, DFT calculations were performed to uncover the reaction mechanism of SRR on SACs. As shown in Fig. 7(h), structure models of FeN_4, CuN_4, and N-C catalysts were established. A SRR process was proposed based on these models

$$S_4^{2-} + * \rightarrow S_2^- + {}^*S_2^- \quad (1)$$

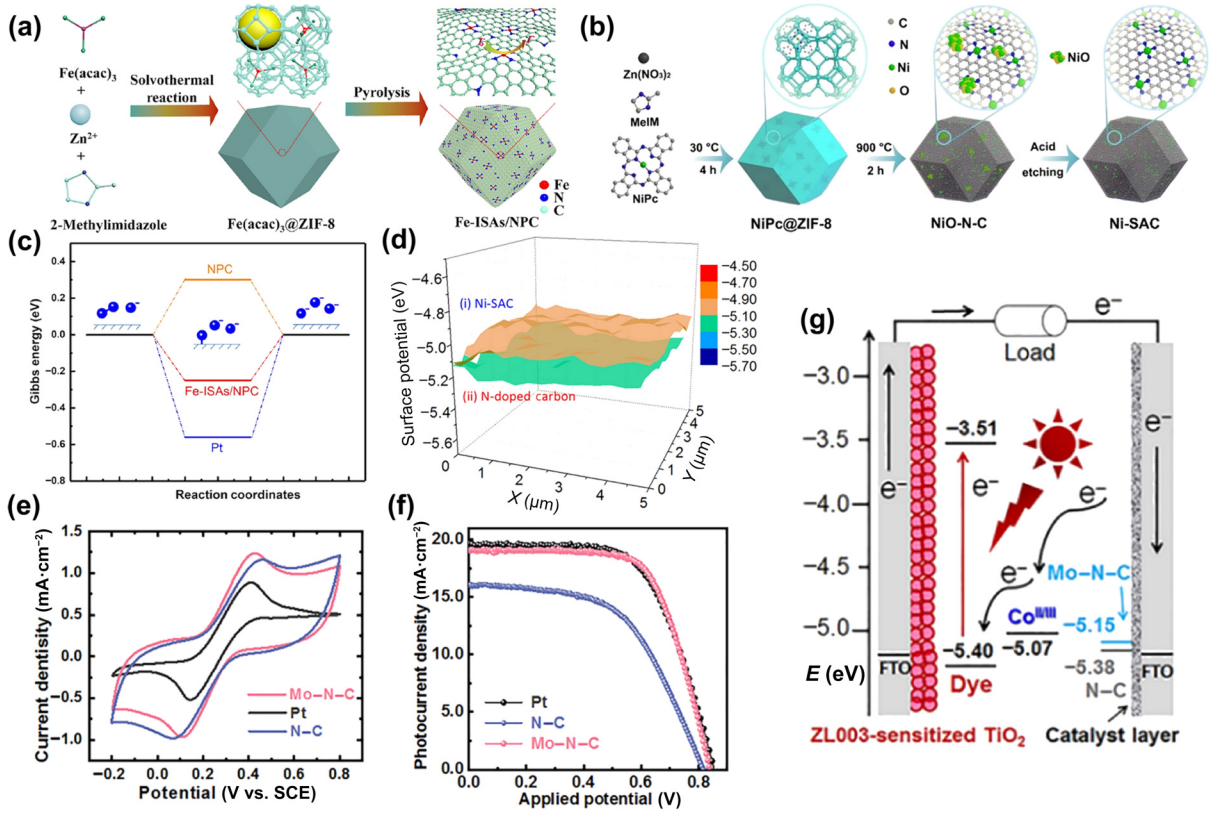

Figure 6 (a) Schematic illustrating the preparation of Fe-ISAs/NPC. (b) Schematic diagram of the synthesis route of Ni-SAC. (c) Free energy diagram for the IRR on the surfaced of NPC, Fe-ISAs/NPC, and Pt (111) at an electrode potential of 0.54 V. Reproduced with permission from Ref. [27], © Elsevier Ltd. 2021. (d) Relative surface potential maps of Ni-SAC and N-C catalysts deposited on an FTO substrate. Reproduced with permission from Ref. [22], © American Chemical Society 2021. (e) CV curves of three different catalysts with respect to the $Co^{3+}/^{2+}(bpy)_3$ redox couple. (f) *J*–*V* curves of DSCs with various catalysts. (g) Schematic illustration of the photo-generated electron transfer process in the hybrid photovoltaic system. Reproduced with permission from Ref. [24], © American Chemical Society 2022.

Table 1 Photovoltaic parameters of DSCs employing various CSAM-based CEs

Metal of CSAMs	Materials	V_{oc} (V)	J_{sc} (mA·cm^{-2})	FF (%)	PCE (%)	Ref.
Pt	Pt/α-MoC@CS	0.785	18.86	66.67	9.87	[23]
Co	SGZ-800	0.83	12.99	73.54	7.89	[113]
Co	Co-S/C-SAC	0.80	13.24	78.00	8.18	[112]
Co	CoN_4/GN	0.72	17.32	67.36	8.40	[111]
Co	$Co/Co_1P_1N_3$	0.725	16.53	71.01	8.51	[114]
Co	Co-NC SACs-900	0.77	17.11	70.16	9.25	[110]
Ti	Ti_1/NC-SAC	0.78	16.71	63.00	8.21	[115]
Ti	Ti_1/rGO	0.83	15.38	65.00	8.29	[26]
Fe	Fe-ISAs/NPC	0.69	17.76	65.00	8.06	[27]
Ni	Ni-SAC	0.715	15.87	67.80	7.68	[22]
Mo	Mo-N-C	0.837	19.02	67.30	10.71	[24]

$$*S_2^- + e^- \rightarrow S^- + *S^-$$
$$*S_2^- + e^- \rightarrow S_2^{2-} + * \quad (2)$$

$$*S^- + e^- \rightarrow * + S^{2-} \quad (3)$$

*represents the adsorption sites on the catalyst surface. The second step reaction has two possible pathways. After the S_2^- anion is adsorbed on the catalyst surface, there are two possible reduction reactions, namely 2-1 and 2-2. If the 2-1 pathway is the dominant reaction step, the product will continue to undergo further reduction in step 3. Therefore, when 2-1 is the intermediate reaction step, the final product will be S^{2-}, whereas if 2-2 is the intermediate step, the final product will be S_2^{2-}. The reaction step of 2-1 leads to a higher degree of polysulfide reduction, making it more favorable for QDSCs. The electronic properties of the S_4^{2-} adsorbed on the catalyst surface were computed and presented in Fig. 7(i). It was observed that the electron transfer between S_4^{2-} and FeN_4 was more significant than that of CuN_4 or N-C catalysts, indicating that the FeN_4 SAC was more effective for S_4^{2-} adsorption. Figures 7(j) and 7(k) illustrate the free energy of the SRR for the three kinds of catalysts. For the CuN_4 SAC, not only is the

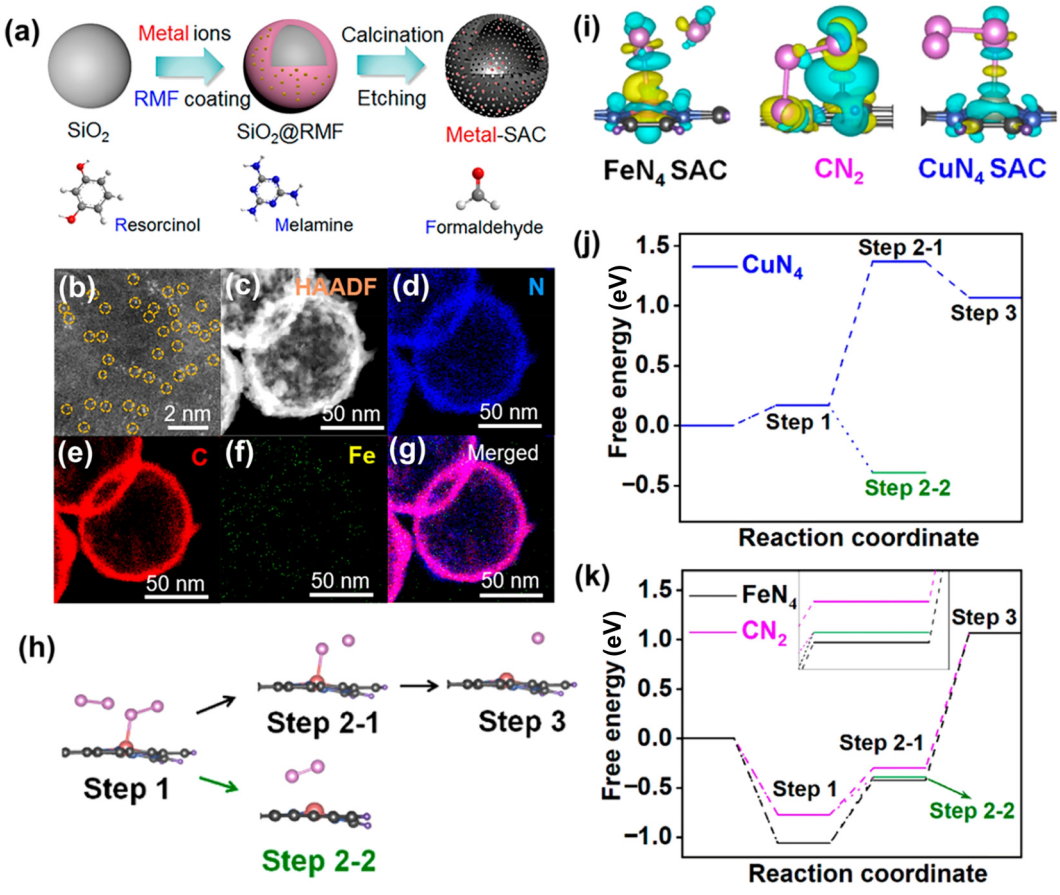

Figure 7 (a) Schematic illustration of the synthesis procedure for Fe-SACs. (b) HAADF-STEM image of Fe SAC, where Fe atoms were marked by circles. (c)–(g) HAADF-STEM image and the corresponding elemental mappings of the Fe-N-C sample. (h) Diagram for the reduction reaction processes of S_4^{2-} anions on the catalysts. (i) The differential charge density distribution for S_4^{2v} adsorbed on the FeN_4, C-N, and CuN_4, respectively. (j) and (k) Reaction free energy diagrams for the reduction of S_4^{2-} to S^{2-} anions on the CuN_4, N-C and FeN_4, respectively. Reproduced with permission from Ref. [25], © American Chemical Society 2023.

adsorption of S_4^{2-} unfavorable (step 1), but also the second step tends to proceed via the 2-2 reaction pathway, producing the product with a lower reduction state, S_2^{2-}. On the other hand, both the FeN_4 SAC and N-C catalysts are favorable for the adsorption of S_4^{2-}, especially the FeN_4 SAC. Furthermore, the second step reaction is also favorable for FeN_4 SAC, making S^{2-} the preferred product for FeN_4 SAC. This result demonstrates that FeN_4 SAC exhibits higher catalytic activity for polysulfide reduction. Finally, we further tested the photovoltaic performance of ZnCuInSe QDSCs based on the Fe-SAC-based photocathode, and achieved the highest PCE of 13.70%.

Similarly, Yun's team employed electrospinning technology to prepare Co SAC anchored on multichannel carbon fibers, denoted as CoN_4@MPCF, as illustrated in Fig. 8(a) [121]. This material was utilized as the CE of Zn-Cu-In-Se QDSCs. To thoroughly investigate the influence of CoN4@MPCF on the SRR, the team conducted detailed DFT calculations.

As shown in Fig. 8(b), a structure model was constructed where a Co single atom coordinated with four N atoms and anchored on a porous carbon substrate, representing the CoN_4@MPCF structure. The charge density analysis (Fig. 8(c)) revealed that in the CoN_4@MPCF model, Co carries a positive charge while N exhibits a negative charge. The resulting positively charged Co center facilitates the adsorption of S_4^{2-} through electrostatic attraction. Shown in Fig. 8(d) is the differential charge density of S_4^{2-} adsorbed on CoN_4@MPCF, in which the electron accumulation is depicted in red while the depletion of electron density is green. Significant electron cloud overlap between Co and S atoms was observed, indicating the formation of a Co–S chemical bond, which reduces the electron transfer barrier. Based on these findings, the Zn-Cu-In-Se QDSC devices with CoN_4@MPCF CEs achieved the highest average PCE of 13.39%. These results highlight the significant impact of the central metal atom in the photocathode CSAMs on the catalytic behavior of polysulfides, which in turn influences the photovoltaic performance of QDSCs.

6 CSAMs in perovskite solar cells

CSAMs exhibit excellent potential for regulating the energy levels of charge transport layers, which can effectively optimize the band alignment at interfaces of PSCs. This facilitates the transfer and extraction of photogenerated carriers at the interfaces, not only enhancing the photovoltaic performance of PSCs but also mitigating structural instability issues caused by carrier accumulation at the interfaces. For example, Shi's group reported a pioneering application of CSAMs in C-PSCs [32]. They anchored Ti single atoms onto rGO via oxygen functional groups on the rGO surface (Ti_1-rGO). By comparing the Fermi levels of rGO, Ti_1-rGO and Spiro-OMeTAD (Fig. 9(a)), they found that the energy levels of Ti_1-rGO and Spiro-OMeTAD were better aligned, which effectively reduced carrier recombination losses at the interface and lowered the V_{oc} loss. As shown in Fig. 9(b), they constructed devices with the structure FTO/c-TiO_2/mp-TiO_2/perovskite/Spiro-

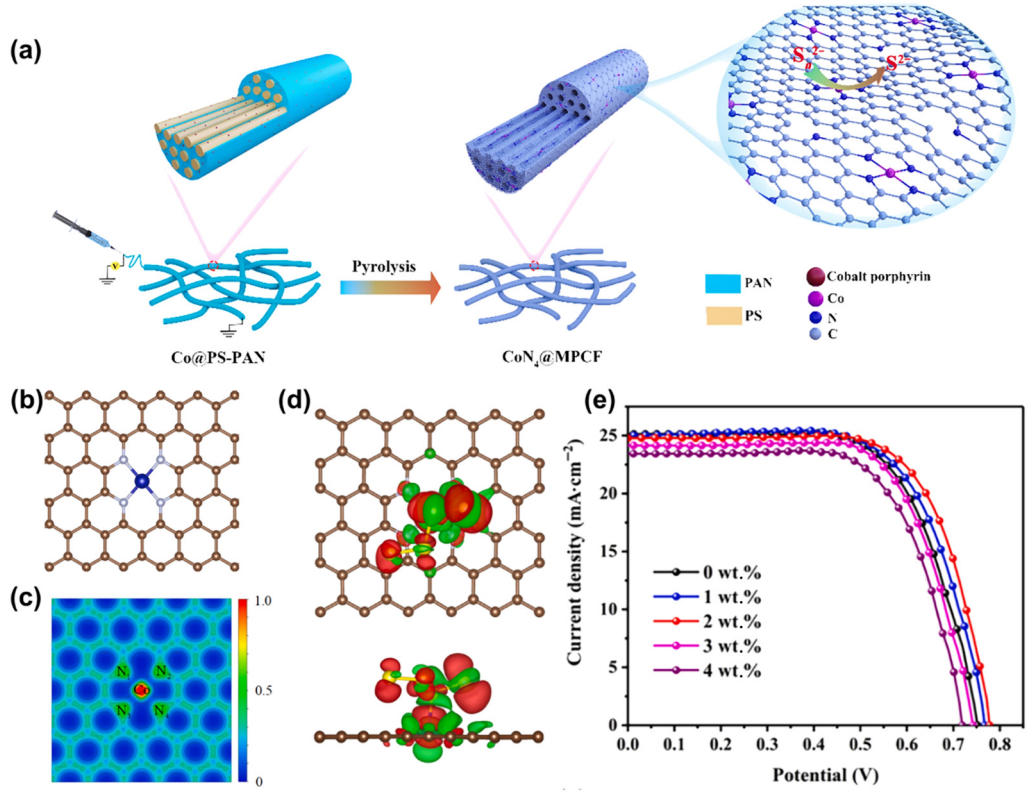

Figure 8 (a) Schematic of the preparation of CoN_4@MPCF. (b) Structure model of CoN_4@MPCF for DFT calculations. (c) 2D charge density of CoN_4@MPCF. (d) 3D isosurface of the differential charge density upon S_4^{2-} adsorption by CoN_4@MPCF. (e) *J*–*V* curves of CoN_4@MPCF based QDSCs. Reproduced with permission from Ref. [121], © Elsevier Ltd. 2025.

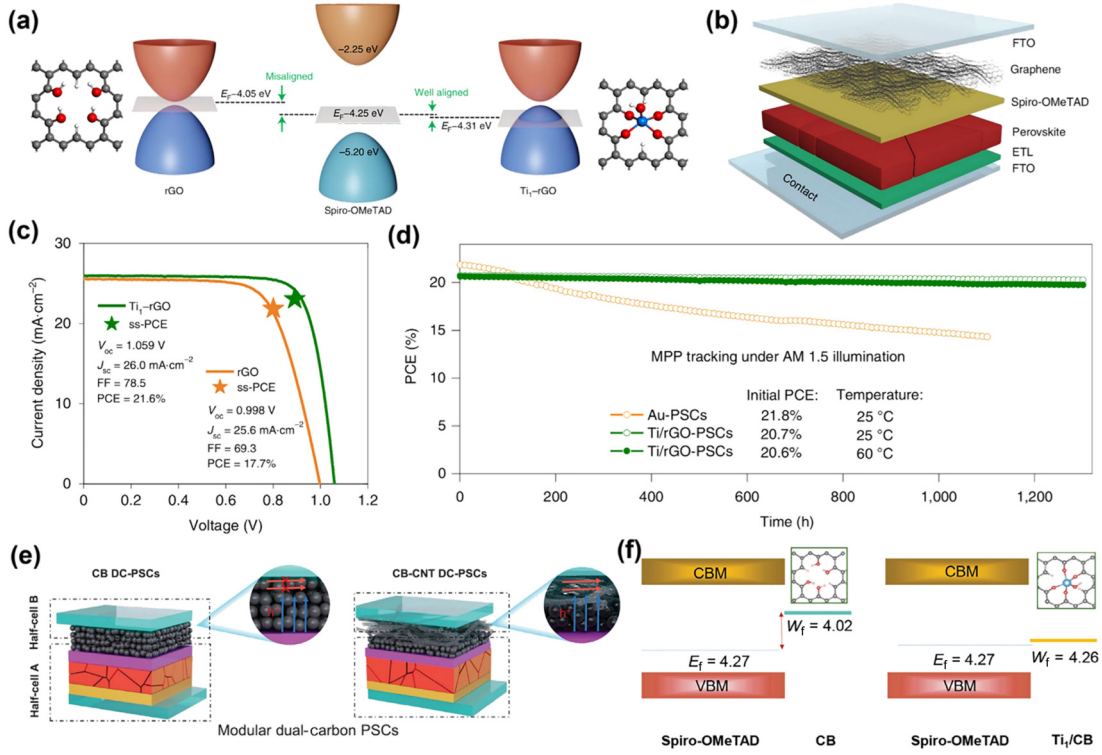

Figure 9 (a) Schematic band alignment between Spiro-OMeTAD and electrode materials (rGO and Ti_1-rGO). (b) Schematic diagram of modular C-PSC structure. (c) *J*–*V* curves of the champion C-PSC device based on rGO and Ti_1-rGO. (d) MPP ageing of Ti_1-rGO-based C-PSC (at 25 and 60 °C, respectively) and PSC based on an Au electrode under an N_2 atmosphere, 1 sun continuous illumination. Reproduced with permission from Ref. [32], © Springer Nature Limited 2021. (e) Schematic diagram of modular dual-carbon perovskite solar cells (DC-PSCs). (f) Energy band alignment between Spiro-OMeTAD and CB or Ti_1/CB electrode materials. Reproduced with permission from Ref. [33], © Wiley-VCH GmbH 2024.

OMeTAD/rGO or Ti_1-rGO/FTO. The device based on Ti_1-rGO achieved a PCE of 21.6%, which significantly outperformed the rGO-based C-PSC with a PCE of 17.7% (Fig. 9(c)). Moreover, stability tests of Ti_1-rGO-based C-PSCs showed remarkable improvements (Fig. 9(d)). After continuous illumination for 1100 h at 25 °C, the PCE of the PSC based on an Au electrode only retained 65% of its initial value, while the Ti_1-rGO-based C-PSC maintained 98% of its initial PCE after 1300 h of continuous illumination. At 60 °C, the Ti_1-rGO-based C-PSC retained 95% of its initial PCE after 1300 h, highlighting the superior stability of carbon materials compared to metal electrodes.

Additionally, the same strategy was applied to load Ti single atoms onto 0D carbon black (Ti_1/CB) to establish effective interfacial contact with the HTL, promoting the extraction of photogenerated holes [33]. One-dimensional carbon nanotubes (CNTs) were also used as dual carbon electrodes to accelerate lateral charge transfer, as shown in Fig. 9(e). The Ti atoms in Ti_1/CB adjust the energy level structure of CB at the molecular level, as shown in Fig. 9(f), resulting in better energy level alignment with Spiro-OMeTAD. This optimization improved charge injection and collection at the interface, effectively reducing charge recombination losses.

Furthermore, they proposed a strategy of directly utilizing CSAMs as the back electrode in C-PSCs [34]. As depicted in Fig. 10(a), the Shi group successfully synthesized Co_1/CN-type CSAMs via a molten salt-mediated thermal pyrolysis approach. Studies revealed that the energy level difference between CN and Spiro-OMeTAD was 0.16 eV, while that between Co_1/CN and Spiro-OMeTAD was only 0.01 eV (Fig. 10(b)). This substantially reduced offset effectively minimizes energy loss during charge transfer and facilitates interfacial hole extraction. Ultimately, as shown in Fig. 10(c), C-PSCs with Co_1/CN as the back electrode achieved a PCE of 22.61%, substantially outperforming the C-N-based PSC (18.35%). Additionally, the Co_1/CN-based C-PSC demonstrated excellent stability, retaining 94.4% of its initial efficiency after 1000 h of continuous illumination (Fig. 10(d)).

Similarly, Guo et al. constructed a novel composite electrode by coupling a commercial carbon electrode with Ni-N co-doped graphene (Ni-NG) [30]. In this structure, the Ni single atoms are uniformly distributed as active sites (Fig. 10(e)). This design enables Ni-NG, with its large specific surface area, to form intimate contact with the perovskite layer, thereby facilitating hole extraction (Fig. 10(f)). Meanwhile, the introduction of Ni single atoms effectively reduces the work function of the material by modifying the electronic structure of graphene, which has been confirmed to enhance hole extraction from the perovskite and suppress electron–hole recombination (Fig. 10(g)). Therefore, through precise engineering of carbon-based electrodes and charge transport layers, CSAMs provide an effective pathway to enhance the performance and stability of PSCs. Their core mechanism is dual: on one hand, they can passivate defects at the interfaces and grain boundaries of the perovskite film, suppressing non-radiative

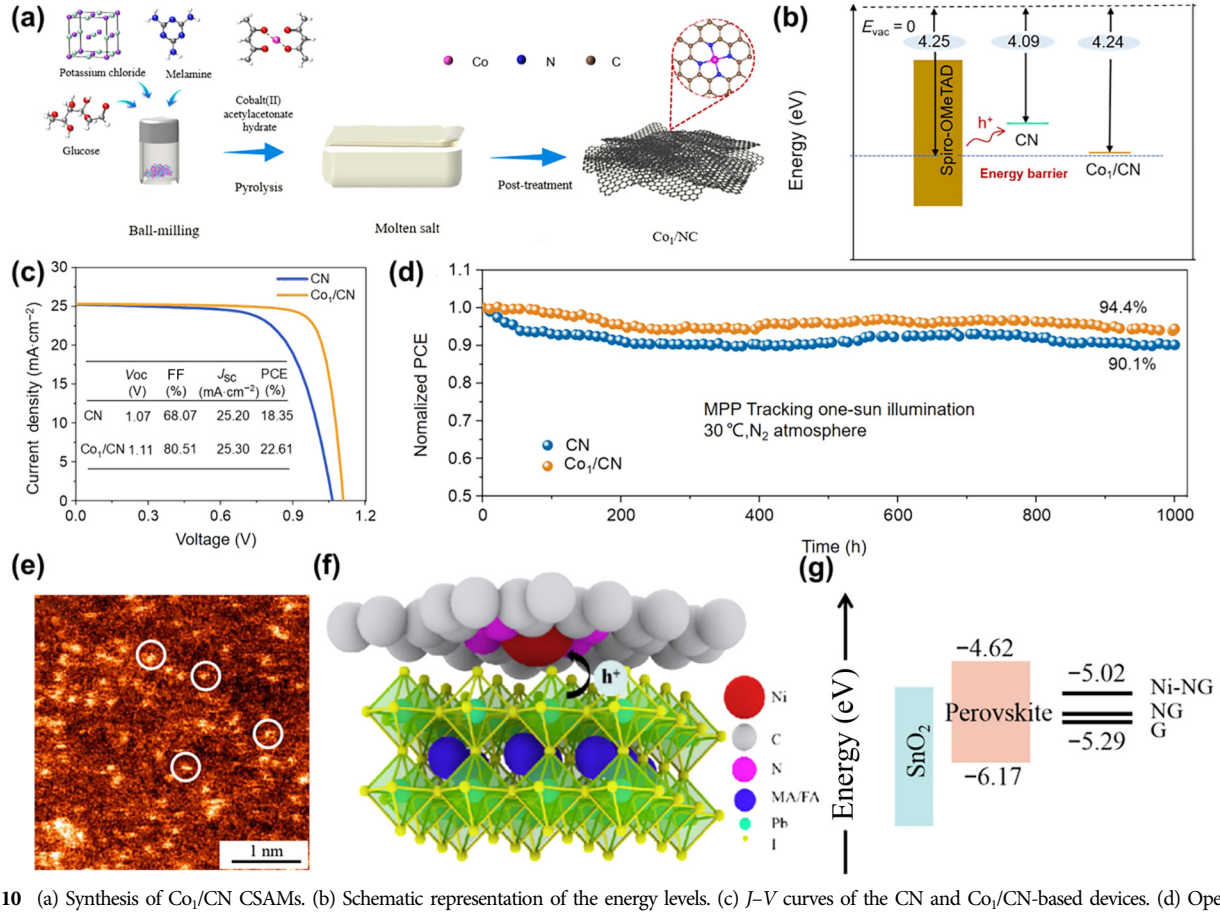

Figure 10 (a) Synthesis of Co_1/CN CSAMs. (b) Schematic representation of the energy levels. (c) *J*–*V* curves of the CN and Co_1/CN-based devices. (d) Operational stability of the encapsulated C-PSC devices. Reproduced with permission from Ref. [34], © Springer Nature Limited 2025. (e) HAADF-STEM image of Ni NG. (f) Schematic diagram of hole extraction from perovskite to composite electrode. (g) The energy band diagram for components used in PSCs based on composite electrode. Reproduced with permission from Ref. [30], © Elsevier Ltd. 2024.

recombination; on the other hand, they optimize energy level alignment, facilitating efficient charge extraction and transport. This synergistic effect of defect and charge management significantly improves the device's PCE and operational stability, propelling C-PSCs closer to commercial viability. Currently, the primary factors limiting the performance and stability enhancement of PSCs include high-density point defects (approximately 10^{15} cm^{-3}) at the perovskite film interface, residual stress, energy level misalignment and interfacial chemical reactions [122]. These issues lead to severe non-radiative recombination of photogenerated carriers and halogen ion migration, significantly reducing the PCE and operational stability of PSCs [123, 124].

To address these challenges, researchers have developed various strategies, such as composition regulation, additive modification, and interface passivation [125–127]. Among them, interface engineering significantly improves device performance by enhancing the interfacial contact between the perovskite and charge transport layers, passivating defects at the perovskite interface, and thereby suppressing carrier recombination at the interface [128]. The top and bottom interface between the perovskite film and charge transfer layers are critical interfaces [129].

In this context, CSAMs can serve as an interfacial modification layer to address the interface issues in PSCs. The metal single atoms and ligand atoms in the carbon support can function as Lewis acid–base sites to passivate defects at the perovskite film interface. Additionally, CSAMs as an interfacial modification layer can effectively improve the energy level alignment between the perovskite layer and the charge transport layers. These characteristics facilitate the transfer and extraction of photogenerated carriers at the perovskite interface, thereby enhancing the performance and stability of the devices.

Our research group developed carbon-dots (CDs) supported Cu single-atom materials (Cu-CDs) via a simple pyrolysis method and employed them as interface modification layers at the buried perovskite bottom interfaces of inverted PSCs [31]. Figure 11(a) displays the X-ray absorption near-edge (XANES) spectra of Cu-CDs, revealing that the absorption edge lies between those of Cu_2O and CuO, indicating a valence state between +1 and +2 for Cu species in Cu-CDs. Furthermore, as shown in Fig. 11(b), the Fourier transform of k^2-weighted extended X-ray absorption fine structure (EXAFS) spectra of the Cu K-edge exhibits no Cu–Cu scattering peak, confirming the atomic dispersion of Cu species in Cu-CDs. Fitting of the EXAFS curves in R-space demonstrated that the first coordination shell of Cu in Cu-CDs consists of a CuN_2O_2 configuration (Fig. 11(c)). To investigate the interaction between Cu single atoms in Cu-CDs and I^- at the perovskite interface, a Cu-CDs-FAI composite was synthesized by reacting Cu-CDs with FAI and structurally characterized using X-ray absorption spectroscopy (XAS). The Fourier-transform EXAFS spectrum (Fig. 11(d)) showed a distinct difference in the second coordination shell

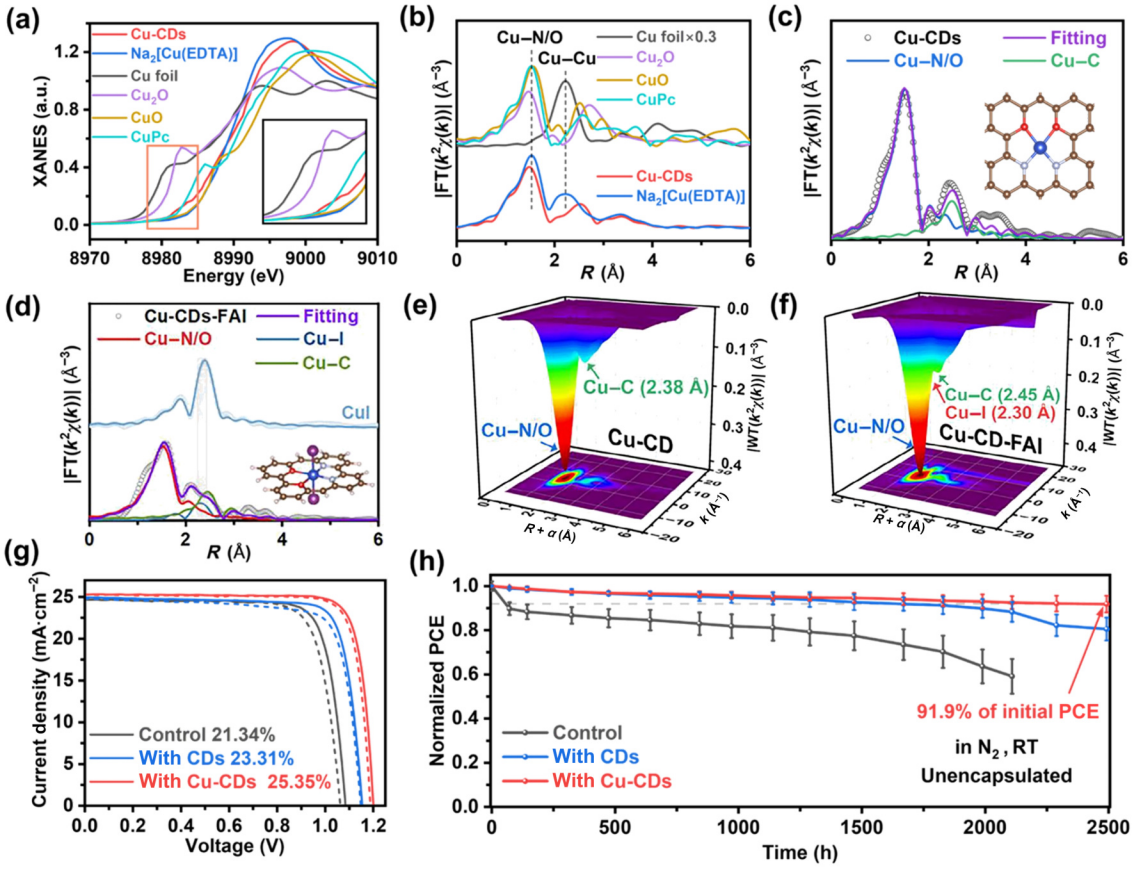

Figure 11 (a) XANES spectra and (b) Fourier transform (FT) of k^2-weighted EXAFS spectra at the Cu K-edge of Cu-CDs, Na_2[Cu(EDTA)], Cu foil, Cu_2O, CuO, and CuPc samples. (c) Cu K-edge EXAFS fitting curves of Cu-CDs in *R* space with the corresponding CuN_2O_2 coordination model shown as an inset. (d) EXAFS fitting curves of Cu-CDs-FAI in R space. The inset in (d) shows the coordination structure of Cu in Cu-CDs-FAI. (e) and (f) Wavelet transform (WT) of Cu-CDs and Cu-CDs-FAI. (g) *J*–*V* curves of the champion devices with and without CDs/Cu-CDs modification at forward (dashed line) and reverse scans (solid line). (h) Long-term storage stability of the unencapsulated device with or without modification at room temperature in a nitrogen atmosphere. Reproduced with permission from Ref. [31], © Wiley-VCH GmbH 2025.

(1.9–2.8 Å) compared to that of pristine Cu-CDs (Fig. 11(c)), suggesting an altered coordination environment around Cu centers due to the incorporation of iodine. Wavelet transform analysis further enhanced the discernibility of these differences (Figs. 11(e) and 11(f)). Notably, incorporating a Cu–I scattering path in the EXAFS fitting accurately reconstructed the spectral features of the second coordination shell, providing strong evidence for Cu–I bonding. Finally, our research group applied Cu-CDs as an interfacial modification layer between the perovskite layer and the PTAA hole-transport layer in inverted PSCs. Devices modified with Cu-CDs achieved a champion PCE of 25.35%, outperforming CDs-modified (23.31%) and control devices (21.34%) (Fig. 11(g)). Moreover, Cu-CDs-based PSCs exhibited significantly improved stability; unencapsulated devices retained 91.9% of their initial PCE after 2500 h under N_2 atmosphere at room temperature, whereas the control devices degraded to 60% of their initial efficiency within 2100 h (Fig. 11(h)). These results demonstrate that the presence of Cu-CDs at the interface enhances both the photovoltaic performance and structural stability of PSCs.

Therefore, as an interface modification layer material in PSCs, CSAMs can effectively enhance both the photovoltaic performance and stability of the devices. The metal single atoms in CSAMs can interact with halogen ions at the interface of PSCs, effectively reducing halogen vacancy defects while suppressing the migration of halogen ions, thereby strengthening the stability of the buried interface in PSCs.

7 Conclusions and outlooks

CSAMs, characterized by their atomically dispersed active sites, unique coordination environments, and tunable electronic structures, offer novel solutions to the efficiency bottlenecks and stability challenges inherent in photovoltaic devices. This review systematically elaborates for the first time on how tailoring the electronic structure and metal atom coordination environment of CSAMs influences their interactions with photovoltaic materials, thereby affecting charge separation, transport, injection, catalysis, and stability mechanisms in solar cells. The atomic precision afforded by CSAMs allows for control over interfacial energetics and reaction kinetics, directly addressing the core issues limiting the efficiency and stability of DSCs, QDSCs and PSCs.

Despite the immense potential CSAMs show in novel solar cells, their practical application faces multiple challenges in synthesis processes, structural design, mechanistic understanding, and long-term stability.

Precise control of synthesis processes: The core difficulty in preparing CSAMs lies in suppressing metal atom agglomeration and achieving a homogeneous coordination structure.

Complexity of device interface engineering: The application of CSAMs in photovoltaic devices requires addressing multiple issues, such as interfacial contact, energy level alignment, and charge transport. Therefore, the substrate structure, coordination environment, and electrical properties of CSAMs must be meticulously designed to optimize the kinetics of carrier transport and reaction processes at the device interfaces.

Mechanistic research and performance optimization: The mechanisms of how CSAMs function in photovoltaic devices are not yet fully understood, which hinders the targeted optimization of materials. For instance, in DSCs and QDSCs, it remains challenging to distinguish between catalytically active sites and to design experiments that can decouple the contributions of single atoms from those of the carbon support. In PSCs, the influence of single-atom sites on charge transfer kinetics is unclear and has not been validated by *in situ* experiments.

Long-term stability challenges: Photovoltaic devices are subjected to external energy stimuli such as light, heat and electricity during operation. Although CSAMs themselves exhibit excellent stability, their long-term impact on the performance of photovoltaic devices still requires more detailed research.

In response to the multiple challenges faced in applying CSAMs to photovoltaics, future research must adopt an integrated strategy that merges mechanistic understanding with engineering practice. From the perspective of mechanistic insight, the core lies in achieving predictive design of CSAMs. This requires a deep understanding of the dynamic evolution of single-atom sites under realistic operating conditions (light, bias, heat) and the establishment of quantitative structure–function relationships between the coordination structures of CSAMs and their functions such as charge extraction and defect passivation. To this end, there is an urgent need to develop advanced characterization techniques capable of performing *in situ* atomic-scale observation. From a practical application standpoint, scalable synthesis and device integration are key to industrialization: On the one hand, methods for the batch synthesis of CSAMs with uniform active sites must be developed; on the other hand, CSAMs should be applied as multifunctional interlayers in photovoltaic devices. In PSCs, this involves synergistically regulating energy level alignment, promoting charge transport, and suppressing interfacial degradation. In DSCs and QDSCs, the design of CSAMs as CEs or transport layers must be optimized to comprehensively enhance PCE and stability. Ultimately, we believe that CSAMs hold the potential to evolve from novel laboratory materials into foundational components for constructing the next generation of high-performance and highly stable photovoltaic devices.

Data availability

All data needed to support the conclusions in the paper are presented in the manuscript.

Acknowledgements

This work was financially supported by the National Natural Science Foundation of China (No. 21771019) and the Fundamental Research Funds for the Central Universities of China (No. buctrc202023).

Declaration of competing interest

All the contributing authors report no conflict of interests in this work.

Author contribution statement

Z. D.: Data curation, writing manuscript. Y. W.: Data curation, writing manuscript. W. F.: Data curation, writing manuscript. W. Q. L.: Writing manuscript. C. R. P.: Data curation. M. H.: Revising manuscript. X. Y.: Project proposal, funding acquisition, revising manuscript. L. Y. W.: Project administration, funding acquisition. All the authors have approved the final manuscript.

Use of AI statement

None.

References

[1] Mathew, S.; Yella, A.; Gao, P.; Humphry-Baker, R.; Curchod, B. F. E.; Ashari-Astani, N.; Tavernelli, I.; Rothlisberger, U.; Nazeeruddin, M. K.; Grätzel, M. Dye-sensitized solar cells with 13% efficiency achieved through the molecular engineering of porphyrin sensitizers. *Nat. Chem.* **2014**, *6*, 242–247.

[2] Zhang, Z. Y.; Song, H.; Wang, W. R.; Rao, H. S.; Fang, Y. P.; Pan, Z. X.; Zhong, X. H. Dual ligand capped quantum dots improving loading amount for high-efficiency quantum dot-sensitized solar cells. *ACS Energy Lett.* **2023**, *8*, 647–656.

[3] Dong, Z.; Lan, Y. H.; Wang, S. S.; Men, J.; Lyu, W. Q.; Zhang, J. B.; Wang, J. J.; Huang, Z. G.; He, M.; Lin, Y. et al. Defect passivation via a bidentate anchoring molecule enables efficient and stable perovskite solar cells. *ACS Appl. Mater. Interfaces* **2025**, *17*, 47243–47251.

[4] Du, J.; Du, Z. L.; Hu, J. S.; Pan, Z. X.; Shen, Q.; Sun, J. K.; Long, D. H.; Dong, H.; Sun, L. T.; Zhong, X. H. et al. Zn–Cu–In–Se quantum dot solar cells with a certified power conversion efficiency of 11.6%. *J. Am. Chem. Soc.* **2016**, *138*, 4201–4209.

[5] Law, M.; Greene, L. E.; Johnson, J. C.; Saykally, R.; Yang, P. D. Nanowire dye-sensitized solar cells. *Nat. Mater.* **2005**, *4*, 455–459.

[6] Yin, X.; Guo, Y. J.; Xue, Z. S.; Xu, P.; He, M.; Liu, B. Performance enhancement of perovskite-sensitized mesoscopic solar cells using Nb-doped TiO_2 compact layer. *Nano Res.* **2015**, *8*, 1997–2003.

[7] Zai, H. C.; Yang, P. F.; Su, J.; Yin, R. Y.; Fan, R. D.; Wu, Y. T.; Zhu, X.; Ma, Y.; Zhou, T.; Zhou, W. T. et al. Wafer-scale monolayer MoS_2 film integration for stable, efficient perovskite solar cells. *Science* **2025**, *387*, 186–192.

[8] Dong, Z.; Wang, J. D.; Men, J.; Zhang, J. W.; Wu, J. P.; Lin, Y.; Xie, X. Y.; Wang, J. J.; Zhang, J. B. High-quality TiO_2 electron transport film prepared via vacuum ultraviolet illumination for $MAPbI_3$ perovskite solar cells. *Inorg. Chem.* **2024**, *63*, 5709–5717.

[9] Li, Q.; Zheng, Y. C.; Wang, H. N.; Liu, X. Y.; Lin, M. Y.; Sui, X. Y.; Leng, X. S.; Liu, D.; Wei, Z. P.; Song, M. Y. et al. Graphene-polymer reinforcement of perovskite lattices for durable solar cells. *Science* **2025**, *387*, 1069–1077.

[10] Gawande, M. B.; Fornasiero, P.; Zbořil, R. Carbon-based single-atom catalysts for advanced applications. *ACS Catal.* **2020**, *10*, 2231–2259.

[11] Duan, Y. X.; Xia, Y. M.; Ling, Y. X.; Zhou, S. J.; Liu, X. H.; Lan, Y. H.; Yin, X.; Yang, Y. S.; Yan, X. Y.; Liang, M. H. et al. Regulating second-shell coordination in cobalt single-atom catalysts toward highly selective hydrogenation. *ACS Nano* **2024**, *18*, 21326–21335.

[12] Xie, X. Y.; Shang, L.; Xiong, X. Y.; Shi, R.; Zhang, T. R. Fe single-atom catalysts on MOF-5 derived carbon for efficient oxygen reduction reaction in proton exchange membrane fuel cells. *Adv. Energy Mater.* **2022**, *12*, 2102688.

[13] Qi, Z. J.; Zhou, Y.; Guan, R. N.; Fu, Y. S.; Baek, J. B. Tuning the coordination environment of carbon-based single-atom catalysts via doping with multiple heteroatoms and their applications in electrocatalysis. *Adv. Mater.* **2023**, *35*, 2210575.

[14] Li, C.-F.; Pan, W.-G.; Zhang, Z.-R.; Wu, T. Recent progress of single-atom photocatalysts applied in energy conversion and environmental protection. *Small* **2023**, *19*, 2300460.

[15] Li, J.; Zhang, M.; Wang, Y. Y.; Lv, W. X.; Xu, Z. R.; Wang, B. B.; Huang, R. Q.; Mei, B. B.; Wang, Y. Regulating the atomic active center by covalent organic framework-derived photothermal nanozyme to arm self-gelling powder for bacterial wound healing. *ACS Nano* **2024**, *18*, 35606–35619.

[16] Chen, Y. J.; Ji, S. F.; Chen, C.; Peng, Q.; Wang, D. S.; Li, Y. D. Single-atom catalysts: Synthetic strategies and electrochemical applications. *Joule* **2018**, *2*, 1242–1264.

[17] Ling, Y. X.; Ge, H. D.; Chen, J. W.; Zhang, Y. Q.; Duan, Y. X.; Liang, M. H.; Guo, Y. J.; Wu, T. S.; Soo, Y. L.; Yin, X. et al. General strategy toward hydrophilic single atom catalysts for efficient selective hydrogenation. *Adv. Sci.* **2022**, *9*, 2202144.

[18] Chen, J. W.; Xia, Y. M.; Ling, Y. X.; Liu, X. H.; Li, S. Y.; Yin, X.; Zhang, L. P.; Liang, M. H.; Yan, Y. M.; Zheng, Q. et al. Zn single-atom catalysts enable the catalytic transfer hydrogenation of α,β-unsaturated aldehydes. *Nano Lett.* **2024**, *24*, 5197–5205.

[19] Fei, H. L.; Dong, J. C.; Feng, Y. X.; Allen, C. S.; Wan, C. Z.; Volosskiy, B.; Li, M. F.; Zhao, Z. P.; Wang, Y. L.; Sun, H. T. et al. General synthesis and definitive structural identification of MN_4C_4 single-atom catalysts with tunable electrocatalytic activities. *Nat. Catal.* **2018**, *1*, 63–72.

[20] Wei, P. K.; Chen, X.; Wu, G. Z.; Li, J.; Yang, Y.; Hao, Z. W.; Zhang, X.; Li, J.; Liu, L. Recent advances in cobalt-, nickel-, and iron-based chalcogen compounds as counter electrodes in dye-sensitized solar cells. *Chin. J. Catal.* **2019**, *40*, 1282–1297.

[21] Wang, S. X.; Tian, J. J. Recent advances in counter electrodes of quantum dot-sensitized solar cells. *RSC Adv.* **2016**, *6*, 90082–90099.

[22] Lin, D.; Jiang, R.; Ma, P.; Hong, S.; Cheng, Z. H.; Guo, J. F.; Xu, R.; Lin, Y.; Zhao, Y. Y.; Yin, X. et al. Nickel-based single-atom catalyst toward triiodide reduction reaction in hybrid photovoltaics. *ACS Sustain. Chem. Eng.* **2021**, *9*, 4256–4261.

[23] Yao, J. X.; Wang, J.; Wang, W.; Meng, Y.; Wang, H. B.; Lu, S. B.; Du, F.; Yang, L.; Zuo, X. Q.; Li, G. α-MoC@CS carrier modulated platinum single atoms for high-efficient solar cells. *Appl. Surf. Sci.* **2023**, *611*, 155582.

[24] Liu, X. H.; Wang, H. H.; Li, W. D.; Chen, J. W.; Fang, J. Q.; Yan, X. Y.; Mi, S.; Hong, S.; Lei, M.; Yin, X. et al. Molybdenum-single atom catalyst for high-efficiency cobalt(III)/(II)-mediated hybrid photovoltaics. *ACS Appl. Energy Mater.* **2022**, *5*, 12991–12998.

[25] Li, L. N.; Lin, Y.; Xia, Y. M.; Lin, D.; Yang, X.; Fang, J. Q.; Liu, X. H.; Chen, J. W.; Yin, X.; Ma, C. Y. et al. Fe single atom catalysts promoting polysulfide redox reduction in quantum dot photovoltaics. *Nano Lett.* **2023**, *23*, 5123–5130.

[26] Liang, S. X.; Zhu, C.; Zhang, N. T.; Zhang, S.; Qiao, B. T.; Liu, H.; Liu, X. Y.; Liu, Z.; Song, X. D.; Zhang, H. M. et al. A novel single-atom electrocatalyst Ti_1/rGO for efficient cathodic reduction in hybrid photovoltaics. *Adv. Mater.* **2020**, *32*, 2000478.

[27] Li, L.; Shi, J.; Zhang, L. S.; Zhao, K. F.; Li, X. T.; Zhang, W. M.; Hagfeldt, A.; Yun, S. N. An experimental and theoretical exploration of the role of tri-element metal-nonmetal nanohybrids in photovoltaics. *Chem. Eng. J.* **2021**, *413*, 127491.

[28] Wang, J. D.; Dong, Z.; Wang, J. J.; Zhang, J. W.; Zhai, Z. Y.; Qiu, F. Z.; Wu, J. P.; Lin, Y.; Zhang, J. B. Room-temperature processed TiO_2 to construct composite electron transport layers for efficient planar perovskite solar cells. *J. Mater. Chem. A* **2023**, *11*, 22206–22215.

[29] Zhao, C. X.; Shu, J. F.; Fang, J. Q.; Luo, S. X.; Guo, Y. J.; Xu, P.; Feng, J.; He, M.; Tan, Z. A.; Yin, X. et al. Interface modification using Li-doped hollow Titania nanospheres for high-performance planar perovskite solar cells. *ACS Appl. Mater. Interfaces* **2023**, *15*, 46925–46932.

[30] Guo, M.; Wei, C. Y.; Liu, C. C.; Zhang, K.; Su, H. J.; Xie, K. Y.; Zhai, P.; Zhang, J.; Liu, L. Composite electrode based on single-atom Ni doped graphene for planar carbon-based perovskite solar cells. *Mater. Des.* **2021**, *209*, 109972.

[31] Shu, J. F.; Liu, Z. X.; Dong, Z.; Yin, X.; Su, G. F.; Ling, Y. X.; Zhang, K.; Zhang, F.; Ma, C. Y.; He, M. et al. Carbon dot-supported single-atom materials boost the efficiency and stability of inverted perovskite solar cells. *Adv. Funct. Mater.* **2025**, *35*, 2506009.

[32] Zhang, C. Y.; Liang, S. X.; Liu, W.; Eickemeyer, F. T.; Cai, X. B.; Zhou, K.; Bian, J. M.; Zhu, H. W.; Zhu, C.; Wang, N. et al. Ti_1–graphene single-atom material for improved energy level

alignment in perovskite solar cells. *Nat. Energy* **2021**, *6*, 1154–1163.
[33] Cheng, J. S.; Ma, H. R.; Shi, Y. Y.; Liu, L. D.; Shang, W. Z.; Liu, W.; Li, S. A.; Li, W. R.; Wang, Y. D.; Shi, Y. T. Single-atom Ti decorated carbon black and carbon nanotubes: Modular dual-carbon electrode for optimizing the charge transport kinetics of perovskite solar cells. *Adv. Funct. Mater.* **2024**, *34*, 2409533.
[34] Shi, Y. Y.; Cheng, X. S.; Wang, Y. D.; Li, W. R.; Shang, W. Z.; Liu, W.; Lu, W.; Cheng, J. S.; Liu, L. D.; Shi, Y. T. Atomically dispersed metal atoms: Minimizing interfacial charge transport barrier for efficient carbon-based perovskite solar cells. *Nano-Micro Lett.* **2025**, *17*, 125.
[35] Bati, A. S. R.; Myagmarsereejid, P.; Fronzi, M.; Fan, K. C.; Liu, P. R.; Zhong, Y. L.; Burn, P. L.; Gentle, I. R.; Shaw, P. E.; Batmunkh, M. Atomically doped 2D black phosphorus for efficient and stable perovskite solar cells. *Small Struct.* **2024**, *5*, 2300334.
[36] Zhao, S. L.; Wang, D. W.; Amal, R.; Dai, L. M. Carbon-based metal-free catalysts for key reactions involved in energy conversion and storage. *Adv. Mater.* **2019**, *31*, 1801526.
[37] Zhang, K.; Dang, Q.; Fang, J. Q.; Wu, Y.; Yang, X.; Dong, Z.; Ma, C. Y.; Xu, P.; Yan, X. Y.; He, M. et al. Atomically dispersed dual-metal-site catalysts boost the CO_2 cycloaddition reaction with epoxides. *ACS Appl. Mater. Interfaces* **2026**, *18*, 1586–1594.
[38] Shi, G. S.; Zhang, W. D.; Kang, Y. K.; Zhao, J.; Lu, T. Y.; Yang, C. L.; Chang, M. W.; Shen, Y. L.; Gao, X. Y.; Wu, J. et al. Nanoconfinement promotes CO_2 electroreduction to methanol on a molecular catalyst. *Nat. Commun.* **2025**, *16*, 7359.
[39] Nakamura, M.; Wu, D. S.; Mukoyoshi, M.; Kusada, K.; Hayashi, H.; Toriyama, T.; Yamamoto, T.; Murakami, Y.; Ashitani, H.; Kawaguchi, S. et al. Unraveling element-selective local structures in multielement alloy nanoparticles with EXAFS. *ACS Nanosci. Au* **2025**, *5*, 196–207.
[40] Shang, Y. N.; Xu, X.; Gao, B. Y.; Wang, S. B.; Duan, X. G. Single-atom catalysis in advanced oxidation processes for environmental remediation. *Chem. Soc. Rev.* **2021**, *50*, 5281–5322.
[41] Yang, X. F.; Wang, A. Q.; Qiao, B. T.; Li, J.; Liu, J. Y.; Zhang, T. Single-atom catalysts: A new frontier in heterogeneous catalysis. *Acc. Chem. Res.* **2013**, *46*, 1740–1748.
[42] Lin, L. H.; Chen, Z.; Chen, W. X. Single atom catalysts by atomic diffusion strategy. *Nano Res.* **2021**, *14*, 4398–4416.
[43] Yang, J. Y.; Huang, Y. K.; Qi, H. F.; Zeng, C. B.; Jiang, Q. K.; Cui, Y. T.; Su, Y.; Du, X. R.; Pan, X. L.; Liu, X. Y. et al. Modulating the strong metal-support interaction of single-atom catalysts via vicinal structure decoration. *Nat. Commun.* **2022**, *13*, 4244.
[44] Goyal, N.; Li, F.; Hu, Y. B. Tailoring single-metal atom catalysts: A strategic defect engineering approach for electrochemical reduction reactions. *J. Mater. Chem. A* **2024**, *12*, 19685–19719.
[45] Shi, X. X.; Wen, Z. L.; Gu, Q. Q.; Jiao, L.; Jiang, H. L.; Lv, H. F.; Wang, H. W.; Ding, J. N.; Lyons, M. P.; Chang, A. et al. Metal-support frontier orbital interactions in single-atom catalysis. *Nature* **2025**, *640*, 668–675.
[46] Guo, Y. L.; Liang, J. X.; Huang, Y. K.; Yang, J. Y.; Zhang, Q.; Wang, A. Q.; Qiao, B. T.; Li, J.; Zhang, T. Covalent and strong metal–support interactions for robust single-atom catalysts. *Acc. Chem. Res.* **2025**, *58*, 2440–2453.
[47] Peng, S. S.; Nian, Y.; Song, X. R.; Shao, X. B.; Gu, C.; Xing, Z. W.; Qi, S. C.; Tan, P.; Han, Y.; Liu, X. Q. et al. Graphene-anchored sodium single atoms: A highly active and stable catalyst for transesterification reaction. *Nano Res.* **2024**, *17*, 4979–4985.
[48] Cui, Y.; Ren, C. J.; Wu, M. L.; Chen, Y.; Li, Q.; Ling, C. Y.; Wang, J. L. Structure-stability relation of single-atom catalysts under operating conditions of CO_2 reduction. *J. Am. Chem. Soc.* **2024**, *146*, 29169–29176.
[49] Liang, X.; Fu, N. H.; Yao, S. C.; Li, Z.; Li, Y. D. The progress and outlook of metal single-atom-site catalysis. *J. Am. Chem. Soc.* **2022**, *144*, 18155–18174.
[50] Liu, K. Y.; Wang, L. P.; Chen, W. X.; Sun, Z. Y.; Geng, H. L.; Li, Y. Q.; Deng, Z. W.; Jiang, S.; Zhou, B. R.; Yu, K. D. et al. The roadmap of carbon-based single-atom catalysts: Rational design and electrochemical applications. *Rare Met.* **2025**, *44*, 7987–8132.
[51] Wang, M. Y.; Ye, M. F.; Wang, J. Y.; Xu, Y.; Wang, Z. D.; Tong, X. Y.; Han, X. Y.; Zhang, K.; Wang, W. H.; Wu, K. L. et al. Recent advances and applications of single atom catalysts based electrochemical sensors. *Nano Res.* **2024**, *17*, 2994–3013.
[52] O'Neill, B. J.; Jackson, D. H. K.; Lee, J.; Canlas, C.; Stair, P. C.; Marshall, C. L.; Elam, J. W.; Kuech, T. F.; Dumesic, J. A.; Huber, G. W. Catalyst design with atomic layer deposition. *ACS Catal.* **2015**, *5*, 1804–1825.
[53] Zhang, L.; Si, R. T.; Liu, H. S.; Chen, N.; Wang, Q.; Adair, K.; Wang, Z. Q.; Chen, J. T.; Song, Z. X.; Li, J. J. et al. Atomic layer deposited Pt–Ru dual-metal dimers and identifying their active sites for hydrogen evolution reaction. *Nat. Commun.* **2019**, *10*, 4936.
[54] Yan, H.; Cheng, H.; Yi, H.; Lin, Y.; Yao, T.; Wang, C. L.; Li, J. J.; Wei, S. Q.; Lu, J. L. Single-atom Pd_1/graphene catalyst achieved by atomic layer deposition: Remarkable performance in selective hydrogenation of 1,3-butadiene. *J. Am. Chem. Soc.* **2015**, *137*, 10484–10487.
[55] Sun, X.; Dawson, S. R.; Parmentier, T. E.; Malta, G.; Davies, T. E.; He, Q.; Lu, L.; Morgan, D. J.; Carthey, N.; Johnston, P. et al. Facile synthesis of precious-metal single-site catalysts using organic solvents. *Nat. Chem.* **2020**, *12*, 560–567.
[56] Wang, L.; Chen, M. X.; Yan, Q. Q.; Xu, S. L.; Chu, S. Q.; Chen, P.; Lin, Y.; Liang, H. W. A sulfur-tethering synthesis strategy toward high-loading atomically dispersed noble metal catalysts. *Sci. Adv.* **2019**, *5*, eaax6322.
[57] Zhan, Z. H.; Wei, Z. H.; Zhang, Z. T.; Wang, L. P.; Cheong, W. C.; Li, S. H.; Chen, W. X.; Pang, S. P. Precisely designing atomically dispersed catalysts for C–N coupling reactions. *Nano Res. Energy* **2025**, *4*, e9120197.
[58] Li, R. S.; Fan, W. J.; Rao, P.; Luo, J. M.; Li, J.; Deng, P. L.; Wu, D. X.; Huang, W.; Jia, C. M.; Liu, Z. X. et al. Multimetallic single-atom catalysts for bifunctional oxygen electrocatalysis. *ACS Nano* **2023**, *17*, 18128–18138.
[59] Wang, X.; Chen, W. X.; Zhang, L.; Yao, T.; Liu, W.; Lin, Y.; Ju, H. X.; Dong, J. C.; Zheng, L. R.; Yan, W. S. et al. Uncoordinated amine groups of metal-organic frameworks to anchor single Ru sites as chemoselective catalysts toward the hydrogenation of quinoline. *J. Am. Chem. Soc.* **2017**, *139*, 9419–9422.
[60] Xia, C.; Qiu, Y. R.; Xia, Y.; Zhu, P.; King, G.; Zhang, X.; Wu, Z. Y.; Kim, J. Y.; Cullen, D. A.; Zheng, D. X. et al. General synthesis of single-atom catalysts with high metal loading using graphene quantum dots. *Nat. Chem.* **2021**, *13*, 887–894.
[61] Chen, X. Q.; Yu, L.; Wang, S. H.; Deng, D. H.; Bao, X. H. Highly active and stable single iron site confined in graphene nanosheets for oxygen reduction reaction. *Nano Energy* **2017**, *32*, 353–358.
[62] Deng, D. H.; Chen, X. Q.; Yu, L.; Wu, X.; Liu, Q. F.; Liu, Y.; Yang, H. X.; Tian, H. F.; Hu, Y. F.; Du, P. P. et al. A single iron site confined in a graphene matrix for the catalytic oxidation of benzene at room temperature. *Sci. Adv.* **2015**, *1*, e1500462.
[63] Zhang, Z. T.; Sun, Z. Y.; Wei, Z. H.; Chen, Z.; Sun, Q.; Zhan, Z. H.; Li, X. C.; Huang, A. X.; Li, S. H.; Chen, W. X. et al. Rational design of nano and atomically dispersed catalysts for electrocatalytic ammonia synthesis from nitrate. *eChem* **2025**, *1*, 2.
[64] O'Regan, B.; Grätzel, M. A low-cost, high-efficiency solar cell based on dye-sensitized colloidal TiO_2 films. *Nature* **1991**, *353*, 737–740.
[65] Freitag, M.; Teuscher, J.; Saygili, Y.; Zhang, X. Y.; Giordano, F.; Liska, P.; Hua, J. L.; Zakeeruddin, S. M.; Moser, J. E.; Grätzel, M. et al. Dye-sensitized solar cells for efficient power generation under ambient lighting. *Nat. Photonics* **2017**, *11*, 372–378.
[66] Mishra, A.; Fischer, M. K. R.; Bäuerle, P. Metal-free organic dyes for dye-sensitized solar cells: From structure: Property relationships to design rules. *Angew. Chem., Int. Ed.* **2009**, *48*, 2474–2499.
[67] Crossland, E. J. W.; Noel, N.; Sivaram, V.; Leijtens, T.; Alexander-

Webber, J. A.; Snaith, H. J. Mesoporous TiO_2 single crystals delivering enhanced mobility and optoelectronic device performance. *Nature* **2013**, *495*, 215–219.

[68] Cui, J. B.; Ma, P.; Li, W. D.; Jiang, R.; Zheng, L. R.; Lin, Y.; Guo, C.; Yin, X.; Wang, L. Y. Surface active-site engineering in hierarchical PtNi nanocatalysts for efficient triiodide reduction reaction. *Nano Res.* **2021**, *14*, 4714–4718.

[69] Roy-Mayhew, J. D.; Bozym, D. J.; Punckt, C.; Aksay, I. A. Functionalized graphene as a catalytic counter electrode in dye-sensitized solar cells. *ACS Nano* **2010**, *4*, 6203–6211.

[70] Hagfeldt, A.; Boschloo, G.; Sun, L. C.; Kloo, L.; Pettersson, H. Dye-sensitized solar cells. *Chem. Rev.* **2010**, *110*, 6595–6663.

[71] Kalyanasundaram, K. Applications of functionalized transition metal complexes in photonic and optoelectronic devices. *Coord. Chem. Rev.* **1998**, *177*, 347–414.

[72] Wu, J. H.; Lan, Z.; Lin, J. M.; Huang, M. L.; Huang, Y. F.; Fan, L. Q.; Luo, G. G.; Lin, Y.; Xie, Y. M.; Wei, Y. L. Counter electrodes in dye-sensitized solar cells. *Chem. Soc. Rev.* **2017**, *46*, 5975–6023.

[73] Sambur, J. B.; Novet, T.; Parkinson, B. A. Multiple exciton collection in a sensitized photovoltaic system. *Science* **2010**, *330*, 63–66.

[74] Sun, Z. H.; Perez, C. M.; Prezhdo, O. V.; Brutchey, R. L. Colloidal $AInSe_2$ (A = K, Rb, Cs) nanocrystals with tunable crystal and band structures. *ACS Nanosci. Au* **2024**, *4*, 381–390.

[75] Dong, Z.; Men, J.; Wang, J. D.; Zhai, Z. Y.; Xie, X. Y.; Zhang, J. B. Preparation of low-defect aluminum-doped zinc oxide nanostructure-based compact layer by vacuum ultraviolet irradiation for quantum dot-sensitized solar cells. *ACS Appl. Nano Mater.* **2023**, *6*, 23515–23523.

[76] Yang, S. L.; Zhao, P. X.; Zhao, X. C.; Qu, L. T.; Lai, X. C. InP and Sn: InP based quantum dot sensitized solar cells. *J. Mater. Chem. A* **2015**, *3*, 21922–21929.

[77] Men, J.; Dong, Z.; Li, Y. S.; Xie, X. Y.; Zhang, C. X.; Qiao, Y. H.; Zhang, J. B. Low-temperature preparation of high electrical conductivity amorphous compact Zn-doped TiO_2 thin films via vacuum ultraviolet for high efficient solar cells. *J. Solid State Chem.* **2025**, *347*, 125302.

[78] Pan, Z. X.; Rao, H. S.; Mora-Seró, I.; Bisquret, J.; Zhong, X. H. Quantum dot-sensitized solar cells. *Chem. Soc. Rev.* **2018**, *47*, 7659–7702.

[79] Radich, E. J.; Dwyer, R.; Kamat, P. V. Cu_2S Reduced graphene oxide composite for high-efficiency quantum dot solar cells. Overcoming the redox limitations of S_2^-/S_n^{2-} at the counter electrode. *J. Phys. Chem. Lett.* **2011**, *2*, 2453–2460.

[80] Yalcin, M.; Takci, D. K.; Demirel, A. F. Application of Cu_2S and Pt counter electrodes in TiO_2@h-BN nanocomposite fibers-based quantum dot sensitized solar cells (QDSSCs). *J. Mol. Struct.* **2025**, *1339*, 142370.

[81] Han, H. J.; Yuan, X. X.; Zhang, Z. X.; Zhang, J. B. Preparation of a ZIF-67 derived thin film electrode via electrophoretic deposition for efficient electrocatalytic oxidation of vanillin. *Inorg. Chem.* **2019**, *58*, 3196–3202.

[82] Monika, S.; Mahalakshmi, M.; Veerathangam, K.; Pandian, M. S.; Ramasamy, P. Conductive carbon black/CuS composite counter electrode for the enhanced photovoltaic performance of CdS quantum dot sensitized solar cells. *Appl. Phys. A* **2022**, *128*, 228.

[83] Kumar, S.; Maurya, I. C.; Prakash, O.; Srivastava, P.; Das, S.; Maiti, P. Functionalized thermoplastic polyurethane as hole conductor for quantum dot-sensitized solar cell. *ACS Appl. Energy Mater.* **2018**, *1*, 4641–4650.

[84] Zeng, J. J.; Wang, W. R.; Lin, Y.; Zhang, Z. Y.; Li, Z. W.; Rao, H. S.; Pan, Z. X.; Zhong, X. H. Nitrogen-doped mesoporous carbon combined with carbon nanotubes as counter electrode catalysts for quantum dot sensitized solar cells with record efficiency. *Sol. Energy* **2024**, *276*, 112699.

[85] Kojima, A.; Teshima, K.; Shirai, Y.; Miyasaka, T. Organometal halide perovskites as visible-light sensitizers for photovoltaic cells. *J. Am. Chem. Soc.* **2009**, *131*, 6050–6051.

[86] Kim, H. S.; Lee, C. R.; Im, J. H.; Lee, K. B.; Moehl, T.; Marchioro, A.; Moon, S. J.; Humphry-Baker, R.; Yum, J. H.; Moser, J. E. et al. Lead iodide perovskite sensitized all-solid-state submicron thin film mesoscopic solar cell with efficiency exceeding 9%. *Sci. Rep.* **2012**, *2*, 591.

[87] Fu, P.; Yang, D.; Chen, Y. H.; Lu, R. X.; Haque, M. A.; Liu, Y. C.; Han, Y. Y.; Li, H.; Chen, R. T.; Liu, J. Q. et al. Synergistic cooperation between photovoltaic and thermoelectric effects in solar cells. *Energy Environ. Sci.* **2025**, *18*, 7082–7088.

[88] Qu, G. P.; Zhang, L. T.; Qiao, Y.; Gong, S. K.; Ding, Y. J.; Tao, Y. L.; Cai, S. Y.; Chang, X. Y.; Chen, Q.; Xie, P. F. et al. Self-assembled materials with an ordered hydrophilic bilayer for high performance inverted perovskite solar cells. *Nat. Commun.* **2025**, *16*, 86.

[89] Dong, B. T.; Wei, M. Y.; Li, Y. H.; Yang, Y. G.; Ma, W.; Zhang, Y. S.; Ran, Y. B.; Cui, M. J.; Su, Z. R.; Fan, Q. P. et al. Self-assembled bilayer for perovskite solar cells with improved tolerance against thermal stresses. *Nat. Energy* **2025**, *10*, 342–353.

[90] Kim, J. Y.; Lee, J. W.; Jung, H. S.; Shin, H.; Park, N. G. High-efficiency perovskite solar cells. *Chem. Rev.* **2020**, *120*, 7867–7918.

[91] Si, H. N.; Zhao, X.; Zhang, Z.; Liao, Q. L.; Zhang, Y. Low-temperature electron-transporting materials for perovskite solar cells: Fundamentals, progress, and outlook. *Coord. Chem. Rev.* **2024**, *500*, 215502.

[92] Ochoa-Martinez, E.; Bijani-Chiquero, S.; de Yuso, M. D. V. M.; Sarkar, S.; Diaz-Perez, H.; Mejia-Castellanos, R.; Eickemeyer, F.; Grätzel, M.; Steiner, U.; Milić, J. V. Nanocrystalline flash annealed nickel oxide for large area perovskite solar cells. *Adv. Sci.* **2023**, *10*, 2302549.

[93] Xu, Z. Z.; Yin, X.; Guo, Y. J.; Pu, Y.; He, M. Ru-doping in TiO_2 electron transport layers of planar heterojunction perovskite solar cells for enhanced performance. *J. Mater. Chem. C* **2018**, *6*, 4746–4752.

[94] Liu, D. Y.; Kelly, T. L. Perovskite solar cells with a planar heterojunction structure prepared using room-temperature solution processing techniques. *Nat. Photonics* **2014**, *8*, 133–138.

[95] Li, Z.; Sun, X. L.; Zheng, X. P.; Li, B.; Gao, D. P.; Zhang, S. F.; Wu, X.; Li, S.; Gong, J. Q.; Luther, J. M. et al. Stabilized hole-selective layer for high-performance inverted p-i-n perovskite solar cells. *Science* **2023**, *382*, 284–289.

[96] Xing, Z.; Ma, S. X.; Chen, B. W.; An, M. W.; Fan, A. J.; Hu, X. Q.; Wang, Y.; Deng, L. L.; Huang, Q. F.; Kanda, H. et al. Solubilizing and stabilizing C_{60} with N-type polymer enables efficient inverted perovskite solar cells. *Joule* **2025**, *9*, 101817.

[97] Feng, K.; Wang, G. L.; Lian, Q.; Gámez-Valenzuela, S.; Li, B. L.; Ding, R. Q.; Yang, W. L.; Wang, K. L.; Zeng, J.; Zhang, Y. et al. Non-fullerene electron-transporting materials for high-performance and stable perovskite solar cells. *Nat. Mater.* **2025**, *24*, 770–777.

[98] Hong, J.; Kang, C. T.; Huang, R.; Wu, Z. J.; Li, L. C.; Li, X. J.; Rao, H. S.; Pan, Z. X.; Zhong, X. H. Anethole regulated crystallization for high efficiency carbon-based perovskite solar cells. *Adv. Funct. Mater.* **2024**, *34*, 2405374.

[99] Adhikari, R. D.; Patel, M. J.; Baishya, H.; Yadav, D.; Kalita, M.; Alam, M.; Iyer, P. K. Decoding recombination dynamics in perovskite solar cells: An in-depth critical review. *Chem. Soc. Rev.* **2025**, *54*, 3962–4034.

[100] Sharma, R.; Zhang, Q. N.; Nguyen, L. L.; Salim, T.; Lam, Y. M.; Sum, T. C.; Duchamp, M. Effect of air exposure on electron-beam-induced degradation of perovskite films. *ACS Nanosci. Au* **2023**, *3*, 230–240.

[101] Sun, M. L.; Shu, J. F.; Zhao, C. X.; Wu, J. P.; Guo, H. D.; Guo, Y. J.; Yin, X.; Lin, Y.; Tan, Z. A.; He, M. et al. Interface modification with

$CuCrO_2$ nanocrystals for highly efficient and stable planar perovskite solar cells. *ACS Appl. Mater. Interfaces* **2022**, *14*, 13352–13360.

[102] Dong, Z.; Men, J.; Zhang, B. H.; Xie, X. Y.; Huang, Z. G.; Ma, Z. B.; Zhai, Z. Y.; Wang, Y. W.; Zeng, Y. F.; Wu, J. P. et al. Grain boundary defect passivation and iodine migration inhibition for efficient and stable perovskite solar cells. *Electrochim. Acta* **2024**, *507*, 145129.

[103] Dong, Z.; Men, J.; Wang, J. J.; Huang, Z. G.; Zhai, Z. Y.; Wang, Y. W.; Xie, X. Y.; Zhang, C. X.; Lin, Y.; Wu, J. P. et al. Surface crystallization enhancement and defect passivation for efficiency and stability enhancement of inverted wide-bandgap perovskite solar cells. *ACS Appl. Mater. Interfaces* **2024**, *16*, 20661–20669.

[104] Wan, Z.; Li, C.; Jia, C. M.; Su, J.; Li, Z. H.; Chen, Y. K.; Rao, F. W.; Cao, F. F.; Xue, J. Y.; Shi, J. S. et al. Suppressing ion migration through dual interface engineering toward efficient and stable perovskite solar modules. *ACS Energy Lett.* **2025**, *10*, 1585–1595.

[105] Domanski, K.; Correa-Baena, J. P.; Mine, N.; Nazeeruddin, M. K.; Abate, A.; Saliba, M.; Tress, W.; Hagfeldt, A.; Grätzel, M. Not all that glitters is gold: Metal-migration-induced degradation in perovskite solar cells. *ACS Nano* **2016**, *10*, 6306–6314.

[106] Zhang, Z. L.; Li, M. J.; Li, R.; Zhuang, X. M.; Wang, C. L.; Shang, X. N.; He, D. M.; Chen, J. Z.; Chen, C. Suppressing ion migration by synergistic engineering of anion and cation toward high-performance inverted perovskite solar cells and modules. *Adv. Mater.* **2024**, *36*, 2313860.

[107] Fagiolari, L.; Bella, F. Carbon-based materials for stable, cheaper and large-scale processable perovskite solar cells. *Energy Environ. Sci.* **2019**, *12*, 3437–3472.

[108] Pandey, S.; Karakoti, M.; Bhardwaj, D.; Tatrari, G.; Sharma, R.; Pandey, L.; Lee, M. J.; Sahoo, N. G. Recent advances in carbon-based materials for high-performance perovskite solar cells: Gaps, challenges and fulfillment. *Nanoscale Adv.* **2023**, *5*, 1492–1526.

[109] Zaman, Z.; Shahroosvand, H.; Bellani, S.; Bonaccorso, F.; Nazeeruddin, M. K. High-efficiency carbon perovskite solar cells via cathode interface engineering by using CuPc hole-transporting layers. *Angew. Chem., Int. Ed.* **2025**, *64*, e202425191.

[110] Ou, J. H.; Liang, R. T.; Zhang, W. J.; Liu, J.; Xia, G. Z.; Xie, Y. Y.; Liu, K. J.; Yan, W. Y.; Zhang, Q.; Zhou, Y. H. Metal-organic framework-derived nitrogen-coordinated cobalt single-atom catalysts for triiodide reduction reaction in solar cells. *Sol. Energy* **2024**, *272*, 112478.

[111] Cui, X. J.; Xiao, J. P.; Wu, Y. H.; Du, P. P.; Si, R.; Yang, H. X.; Tian, H. F.; Li, J. Q.; Zhang, W. H.; Deng, D. H. et al. A graphene composite material with single cobalt active sites: A highly efficient counter electrode for dye-sensitized solar cells. *Angew. Chem., Int. Ed.* **2016**, *55*, 6708–6712.

[112] Li, N. N.; Zhu, C.; Zhang, J. W.; Jing, H. Y.; Hu, J. W.; Hao, C.; Shi, Y. T. Single-atom-catalyst with abundant Co–S_4 sites for use as a counter electrode in photovoltaics. *Chem. Commun.* **2021**, *57*, 5302–5305.

[113] Jing, H. Y.; Zhao, Z. Y.; Zhang, J. W.; Zhu, C.; Liu, W.; Li, N. N.; Hao, C.; Shi, Y. T.; Wang, D. S. Atomic evolution of metal-organic frameworks into Co–N_3 coupling vacancies by cooperative cascade protection strategy for promoting triiodide reduction. *J. Phys. Chem. C* **2021**, *125*, 6147–6156.

[114] Zhou, D. N.; Xia, Z. M.; Shang, H. S.; Xiao, H.; Jiang, Z. L.; Li, H. J.; Zheng, L. R.; Dong, J. C.; Chen, W. X. A rational design of an efficient counter electrode with the $Co/Co_1P_1N_3$ atomic interface for promoting catalytic performance. *Mater. Chem. Front.* **2021**, *5*, 3085–3092.

[115] Xin, C. C.; Liang, S. X.; Hu, J. W.; Guo, J. Y.; Cheng, X. S.; Shang, W. Z.; Wei, J. Z.; Zhang, S. L.; Liu, W.; Zhu, C. et al. *In-situ* grafting of single-atomic titanium-nitrogen moiety onto carbon nanostructures for efficient photovoltaic devices. *ACS Appl. Mater. Interfaces* **2022**, *14*, 50849–50857.

[116] Du, Z. L.; Pan, Z. X.; Fabregat-Santiago, F.; Zhao, K.; Long, D. H.; Zhang, H.; Zhao, Y. X.; Zhong, X. H.; Yu, J. S.; Bisquert, J. Carbon counter-electrode-based quantum-dot-sensitized solar cells with certified efficiency exceeding 11%. *J. Phys. Chem. Lett.* **2016**, *7*, 3103–3111.

[117] Li, Y.; Zhao, L. L.; Du, Z. L.; Du, J.; Wang, W.; Wang, Y.; Zhao, L. J.; Cao, X. M.; Zhong, X. H. Metal-organic framework derived Co,N-bidoped carbons as superior electrode catalysts for quantum dot sensitized solar cells. *J. Mater. Chem. A* **2018**, *6*, 2129–2138.

[118] Guo, W. X.; Du, Z. L.; Zhao, Q. F.; Zhang, H.; Zhong, X. H. Controlled sulfidation approach for copper sulfide-carbon hybrid as an effective counter electrode in quantum-dot-sensitized solar cells. *J. Phys. Chem. C* **2016**, *120*, 16500–16506.

[119] Lin, Y.; Song, H.; Rao, H. S.; Du, Z. L.; Pan, Z. X.; Zhong, X. H. MOF-derived Co,N Codoped carbon/Ti mesh counter electrode for high-efficiency quantum dot sensitized solar cells. *J. Phys. Chem. Lett.* **2019**, *10*, 4974–4979.

[120] Jiao, S.; Du, J.; Du, Z. L.; Long, D. H.; Jiang, W. Y.; Pan, Z. X.; Li, Y.; Zhong, X. H. Nitrogen-doped mesoporous carbons as counter electrodes in quantum dot sensitized solar cells with a conversion efficiency exceeding 12%. *J. Phys. Chem. Lett.* **2017**, *8*, 559–564.

[121] Li, L.; Pang, Q.; Zhao, K. F.; Wang, S. Y.; Wang, X.; Li, X. T.; Zhang, W. M.; Yun, S. N. Single cobalt atoms anchored on multichannel carbon fibers as counter electrode for quantum dot sensitized solar cells. *Sol. Energy* **2025**, *300*, 113861.

[122] Yan, N.; Fang, Z. M.; Dai, Z. H.; Feng, J. S.; Liu, S. Z. Buried interface-the key issues for high performance inverted perovskite solar cells. *Adv. Funct. Mater.* **2024**, *34*, 2314039.

[123] Zai, H. C.; Ma, Y.; Chen, Q.; Zhou, H. P. Ion migration in halide perovskite solar cells: Mechanism, characterization, impact and suppression. *J. Energy Chem.* **2021**, *63*, 528–549.

[124] Liu, S. W.; Li, J. B.; Xiao, W. S.; Chen, R.; Sun, Z. X.; Zhang, Y.; Lei, X.; Hu, S. F.; Kober-Czerny, M.; Wang, J. N. et al. Buried interface molecular hybrid for inverted perovskite solar cells. *Nature* **2024**, *632*, 536–542.

[125] Li, S. S.; Jiang, Y. Z.; Xu, J.; Wang, D.; Ding, Z. J.; Zhu, T.; Chen, B.; Yang, Y. G.; Wei, M. Y.; Guo, R. J. et al. High-efficiency and thermally stable $FACsPbI_3$ perovskite photovoltaics. *Nature* **2024**, *635*, 82–88.

[126] Park, J.; Kim, J.; Yun, H. S.; Paik, M. J.; Noh, E.; Mun, H. J.; Kim, M. G.; Shin, T. J.; Seok II, S. Controlled growth of perovskite layers with volatile alkylammonium chlorides. *Nature* **2023**, *616*, 724–730.

[127] Lan, Z. R.; Wang, Y. D.; Shao, J. Y.; Ma, D. X.; Liu, Z. H.; Li, D. M.; Hou, Y.; Yao, J. N.; Zhong, Y. W. Surface passivation with diaminopropane dihydroiodide for p-i-n perovskite solar cells with over 25% efficiency. *Adv. Funct. Mater.* **2024**, *34*, 2312426.

[128] Liu, C.; Huang, K. X.; Hu, B. H.; Li, Y. R.; Zhang, L. Z.; Zhou, X. Y.; Liu, Y. L.; Liu, Z. X.; Sheng, Y. F.; Chen, S. et al. Concurrent top and buried surface optimization for flexible perovskite solar cells with high efficiency and stability. *Adv. Funct. Mater.* **2023**, *33*, 2212698.

[129] Wen, B.; Chen, T.; Yin, Q. X.; Xie, J. S.; Dai, C. H.; Lin, R. H.; Zhou, S. C.; Yu, J. C.; Gao, P. Q. Robust chelated lead octahedron surface for efficient and stable perovskite solar cells. *Nat. Commun.* **2024**, *15*, 7720.